DISEASES AND DISORDERS

Small extracellular vesicles from young adipose-derived stem cells prevent frailty, improve health span, and decrease epigenetic age in old mice

Jorge Sanz-Ros[1], Nekane Romero-García[1], Cristina Mas-Bargues[1], Daniel Monleón[2], Juozas Gordevicius[3], Robert T. Brooke[3], Mar Dromant[1], Ana Díaz[1], Aksinya Derevyanko[4], Ana Guío-Carrión[4], Aurora Román-Domínguez[1], Marta Inglés[5], María A. Blasco[4], Steve Horvath[6,7,8], Jose Viña[1], Consuelo Borrás[1]*

Aging is associated with an increased risk of frailty, disability, and mortality. Strategies to delay the degenerative changes associated with aging and frailty are particularly interesting. We treated old animals with small extracellular vesicles (sEVs) derived from adipose mesenchymal stem cells (ADSCs) of young animals, and we found an improvement in several parameters usually altered with aging, such as motor coordination, grip strength, fatigue resistance, fur regeneration, and renal function, as well as an important decrease in frailty. ADSC-sEVs induced proregenerative effects and a decrease in oxidative stress, inflammation, and senescence markers in muscle and kidney. Moreover, predicted epigenetic age was lower in tissues of old mice treated with ADSC-sEVs and their metabolome changed to a youth-like pattern. Last, we gained some insight into the microRNAs contained in sEVs that might be responsible for the observed effects. We propose that young sEV treatment can promote healthy aging.

INTRODUCTION

To add health to the years gained, as well as to promote the ability to live autonomously, is a public health priority in modern societies. The search for strategies to delay the degenerative changes associated with aging and frailty is particularly interesting.

Aging is accompanied by an impairment in the physical condition and an increased risk of frailty (*1*). It is characterized by several changes at the cellular and organismal levels, such as oxidative stress, telomere attrition, or cellular senescence (*2*), that result in a decreased functionality of tissues. These changes are proposed as the main factors that drive age-related conditions, such as sarcopenia or renal failure (*3*, *4*). One of the traits associated with aging is the alteration in intercellular communication. As an individual ages, the extracellular environment changes, with deregulation of important signaling pathways [i.e., insulin–insulin-like growth factor 1 (IGF1) or renin-angiotensin] (*5*) and a chronic proinflammatory status (*6*, *7*). Therefore, cellular function not only depends on cell-autonomous factors but also is affected by the extracellular environment, and its modification can have a great effect on the performance of several tissues (*5*, *8*).

Parabiosis experiments conducted in mice demonstrated that factors present in the blood of a young organism are beneficial for an aged one, improving several parameters affected by aging (*9*–*11*). Moreover, interventions that delay aging on a specific tissue can induce similar changes in distant tissues (*12*–*14*).

Extracellular vesicles (EVs), small vesicles that are released by virtually all cell types, with an innate ability to mediate the transmission of signaling molecules (proteins, small RNAs, and DNA) between cells are among the factors that are involved in the communication between cells (*15*).

Stem cells have intrinsic regenerative effects that are not only mediated by the repopulation of damaged tissue. The releasing of regulatory molecules is also proposed as one of the most important mechanisms in stem cell therapies (*16*, *17*). More specifically, small EVs (sEVs) derived from multiple stem cells have demonstrated their capacity to promote tissue regeneration after several types of damage (*18*, *19*). Compared to stem cells, sEVs are more stable, have no risk of aneuploidy, have a lower chance of immune rejection, and can provide an alternative therapy for various diseases (*20*–*23*).

It is important to consider the way culturing stem cells affects markedly paracrine signals. We previously showed that oxygen tension in culture is one of the most important factors affecting the biological function of sEVs released by these cells (*24*–*26*) and that sEVs derived from mesenchymal stem cells (MSCs) cultured under hypoxic conditions can mediate the transfer of microRNAs (miRNAs) to senescent cells and improve cellular function (*25*). A recent study demonstrated that hypothalamic stem cells modulate aging speed through the release of miRNAs contained in EVs (*27*). sEVs are emerging as a potential therapy in the aging field. It has been recently shown that sEVs can exert proregenerative effects in tissues of old mice and decrease senescence-related damage (*28*–*31*). However, the effect of MSC-derived sEVs on the health span of an aged organism has not been fully addressed. Here, we show that sEVs from young adipose-derived stem cells (ADSC-sEVs) improve several functions that are impaired in old mice. Old mice that received young ADSC-sEVs showed lower levels of frailty and improvements on physical condition tests, fur regeneration, and renal function. ADSC-sEVs induced

[1]Freshage Research Group, Department of Physiology, Faculty of Medicine, University of Valencia, Centro de Investigación Biomédica en Red Fragilidad y Envejecimiento Saludable-Instituto de Salud Carlos III (CIBERFES-ISCIII), INCLIVA, 46010 Valencia, Spain. [2]Department of Pathology, Faculty of Medicine, University of Valencia, CIBERFES, INCLIVA, Avenida Blasco Ibáñez, 15, Valencia, Spain. [3]Epigenetic Clock Development Foundation, Torrance, CA, USA. [4]Telomeres and Telomerase Group, Molecular Oncology Program, Spanish National Cancer Centre, 28029 Madrid, Spain. [5]Freshage Research Group, Department of Physiotherapy, Faculty of Physiotherapy, University of Valencia, CIBERFES, INCLIVA, Avenida Blasco Ibáñez, 15, Valencia Spain. [6]Department of Human Genetics, David Geffen School of Medicine, University of California, Los Angeles, Los Angeles, CA, USA. [7]Department of Biostatistics, Fielding School of Public Health, University of California, Los Angeles, Los Angeles, CA, USA. [8]Altos Labs, San Diego, CA, USA.
*Corresponding author. Email: consuelo.borras@uv.es

proregenerative effects in muscle and kidney of aged mice, as well as a decrease in oxidative stress, inflammation, and senescence markers. Moreover, predicted epigenetic age was lower in tissues of old mice treated with ADSC-sEVs and the metabolome of old mice treated with ADSC-sEVs changed from an old-like pattern to a youth-like one. Last, we gained some insight into the miRNAs contained in sEVs that might be, at least in part, responsible for the effects observed.

RESULTS

ADSCs release sEVs to the culture medium that are delivered to the kidney and muscle of old mice

In the first place, we performed a characterization of the vesicles isolated from the cell culture medium of ADSCs, following the minimal information for studies of extracellular vesicles (MISEV) recommendations for the characterization and functional studies of sEVs (*32*). For this purpose, we performed a nanoparticle tracking analysis (NTA) of the isolated samples from differential ultracentrifugation, showing a mean of 169 nm and a mode of 176 nm (Fig. 1A), concurrent with the definition of sEVs (*32*).

Second, we confirmed the presence of TSG101, a cytosolic protein present in sEVs, using immunoblotting in our samples (Fig. 1B). As we used a little amount (2%) of exosome-depleted fetal bovine serum (FBS) in the culturing of ADSCs, we used it as a negative control of the presence of TSG101. As we were isolating sEVs from the conditioned medium of ADSCs, FBS was the only source of potential contaminating proteins from plasma such as albumin, so we used it as a positive control in the determination of albumin as a contaminant in our samples (Fig. 1B).

Continuing with the characterization of sEVs, we checked for the expression of CD63, a widely used marker from the tetraspanin family in the membrane of sEVs (*33*). Using flow cytometry, we were able to confirm the presence of this marker in the samples (Fig. 1C). Second, we used transmission electron microscopy to measure the size and morphology of the isolated vesicles. We could observe round-shaped vesicles that ranged from 50 to 200 nm in diameter (Fig. 1D). In addition, we found the presence of CD63 in the membrane of the isolated vesicles with immunogold labeling (Fig. 1E).

Last, to demonstrate a direct effect and the uptake of sEVs in our main tissues of interest, we labeled our sEVs with a lipophilic dye (PKH26) and injected them into the bloodstream of old mice. We then fixed the kidney and muscle and evidenced an uptake of the dye in these tissues with immunofluorescence (Fig. 1F).

ADSC-sEVs improve health span and prevent frailty in old mice

As aged organisms typically show impairment in their physical condition and an increased risk of frailty, we designed an experiment to test whether ADSC-sEVs could have a beneficial effect on the physical performance of old mice. Before treatment, we measured total body weight, grip strength, motor coordination, and resistance to fatigue in aged mice, which were recorded as baseline values. Twenty-four hours later, each mouse received an injection of 20 μg of ADSC-sEVs or phosphate-buffered saline (PBS) as a control in the tail vein (day 1). One week later (day 7), the mice received a second injection (as outlined in Fig. 2A).

As physical tests depend on the weight of mice, we measured the total body weight of mice during the experiment, and we did not find differences between groups. In addition, we failed to observe any signs of toxicity (excessive weight loss) during the entire experiment (Fig. 2B). Physical tests were repeated on days 14 and 30 after ADSC-sEV or PBS treatment. On day 14, we could observe an improvement in the strength test on ADSC-sEV–treated mice. The maximum benefit was observed on day 30: Mice treated with ADSC-sEVs showed an improvement in grip strength, motor coordination, and fatigue resistance when compared to controls (Fig. 2, C to E). Sixty days after treatment, the positive effect was lost, and we could not find any differences between groups (table S1). Thus, the protective effects of ADSC-sEVs are transitory.

For a quantitative assessment of frailty, we used a score on the basis of the clinical phenotype of frail humans developed by our group (*34*). This enabled us to classify each mouse as frail or nonfrail at each time point. On day 30, there were no frail mice in the ADSC-sEV–treated group, while the control group shed 40% of frail mice, which is in accordance with previous results in mice of this age (Fig. 2F) (*34*).

Fur density is reduced, and the capacity to regrowth hair becomes impaired with aging (*35*). To check the effect of ADSC-sEVs on the growth of hair, we plucked a square of 1 cm by 1 cm of the dorsal fur of each mouse on day 1 just before injection. On day 14, we observed that most mice treated with ADSC-sEVs had regenerated the entire area. In contrast, mice injected with PBS had a much lower capacity for hair regrowth (Fig. 2, G and H).

To determine possible changes in the renal function, we used plasma values of urea, as it is a well-known marker of kidney function. We obtained plasma samples of each mouse on days 0, 14, 30, and 60 and measured urea levels at each time point. Day 0 levels were used as a baseline. Fourteen days after being injected with ADSC-sEVs, mice showed a decrease in plasma concentration of urea, whereas the control group showed no modification. On day 30, urea levels raised 50% from baseline in the control group. By contrast, the ADSC-sEV group showed a plasmatic urea level like day 0 (Fig. 2I).

In addition, as a control to further test the possible effect of age on the quality of sEVs and ADSCs, we performed a pilot study with old mice treated with ADSC-sEVs isolated from old mice, we did not find any effect of these old-sEVs on physical performance tests, indicating that the age of ADSC donor is essential in the beneficial effects observed (table S2). Moreover, we did not find any effect of the non-EVs fraction on the physical performance of old mice (table S3). To explore the role of ADSC-sEVs on mice of other age groups, we treated young mice (4 to 6 months) with sEVs from young ADSCs. We did not find a beneficial effect of ADSC-sEVs in the physical performance of young mice (table S4), suggesting that sEVs are specifically acting on age-related features. Together, we find that ADSC-sEVs isolated from young mice induce an improvement in the global health span of aged mice.

ADSC-sEVs reverse age-related structural changes in the kidney and muscle of old mice

As an organism begins to age, its tissues suffer from several structural changes, which are detrimental to the normal function of the tissue, such as a loss of regenerative capacity and fibrosis (*2*, *36*). We selected kidney and muscle to test the effect of ADSC-sEVs on tissue structure, as these organs are especially involved in the aging process: Kidney function is one of the functions that age faster in normal individuals (*37*), and muscle function is essential for the activities of daily life and is directly related to frailty (*38*). Therefore, we obtained kidney and muscle from old mice 30 days after treatment with

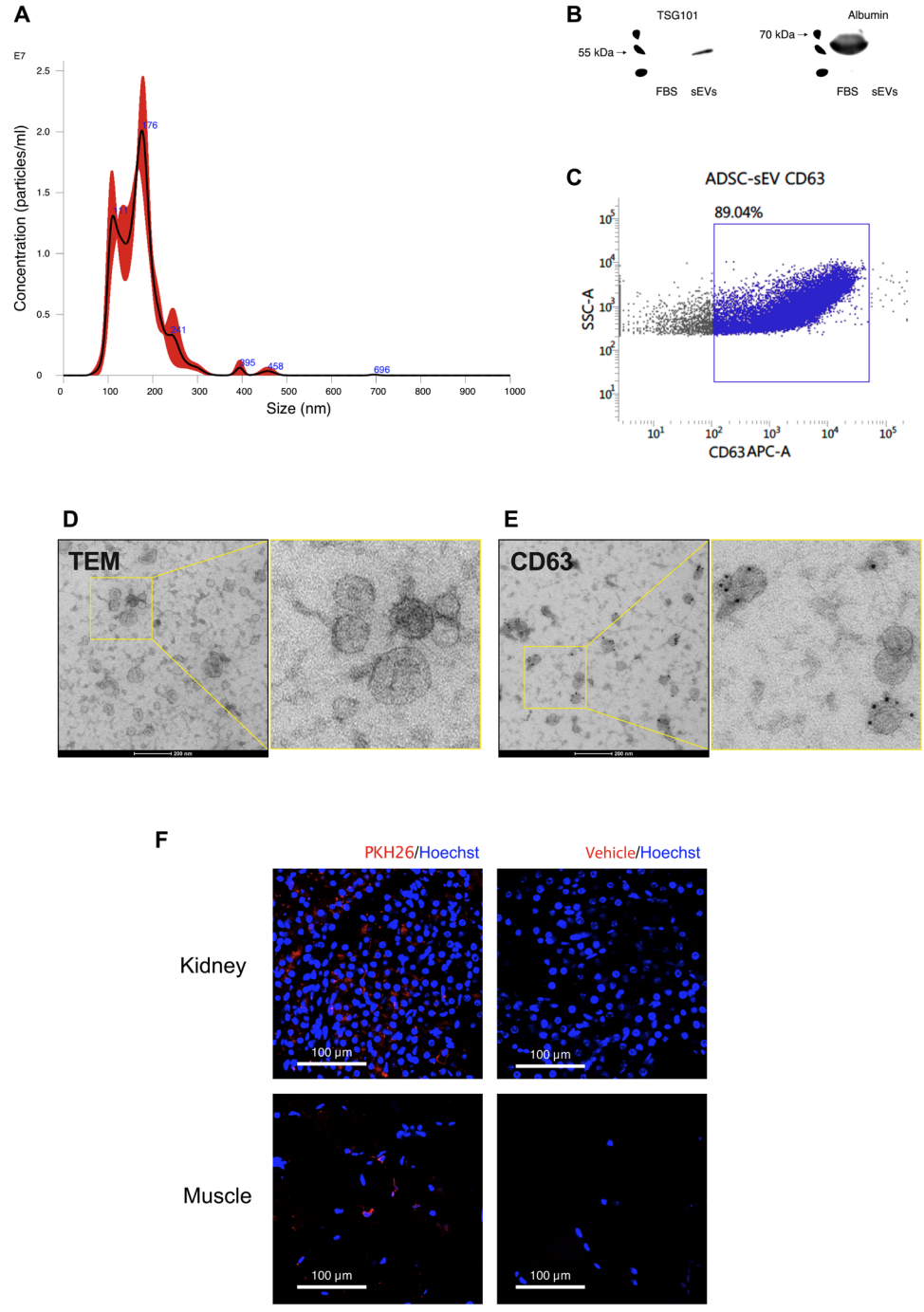

Fig. 1. Characterization of sEVs from ADSC culture medium, which are delivered to kidney and muscle of old mice. (**A**) Nanoparticle tracking analysis (NTA) of sEVs from young ADSCs. (**B**) Western blot image of staining with TSG101 and bovine serum albumin, a sample of purified sEVs from the cell culture medium of ADSCs, and a sample of FBS present in the same medium are shown. (**C**) Flow cytometry determination of CD63 presence in sEVs obtained from the cell culture medium of young ADSCs. (**D** and **E**) Representative image of ADSC-sEVs as observed by transmission electron microscopy (TEM) and CD63 determination with immuno-gold labeling. (**F**) Images of kidney and muscle from old mice treated with PKH26-labeled sEVs from young ADSCs and vehicle as a control.

ADSC-sEVs/PBS. In the kidney, we performed histological analysis of the renal cortex, looking for the presence of tubular atrophy and interstitial fibrosis, two distinctive changes associated with aging that leads to the loss of renal function (*4*). The macroscopic appearance of kidneys was very different between old untreated and treated mice; kidneys isolated from old mice treated with sEVs were more like those isolated from young mice (Fig. 3A). Control mice showed higher tubular atrophy than ADSC-sEV–treated ones, defined by a reduced tubular density and the presence of dilated tubules. Tubular dilation was reduced, and tubular density was higher in mice treated with ADSC-sEVs. We did not observe differences in glomerular density between groups (Fig. 3, B to E). For the study of interstitial

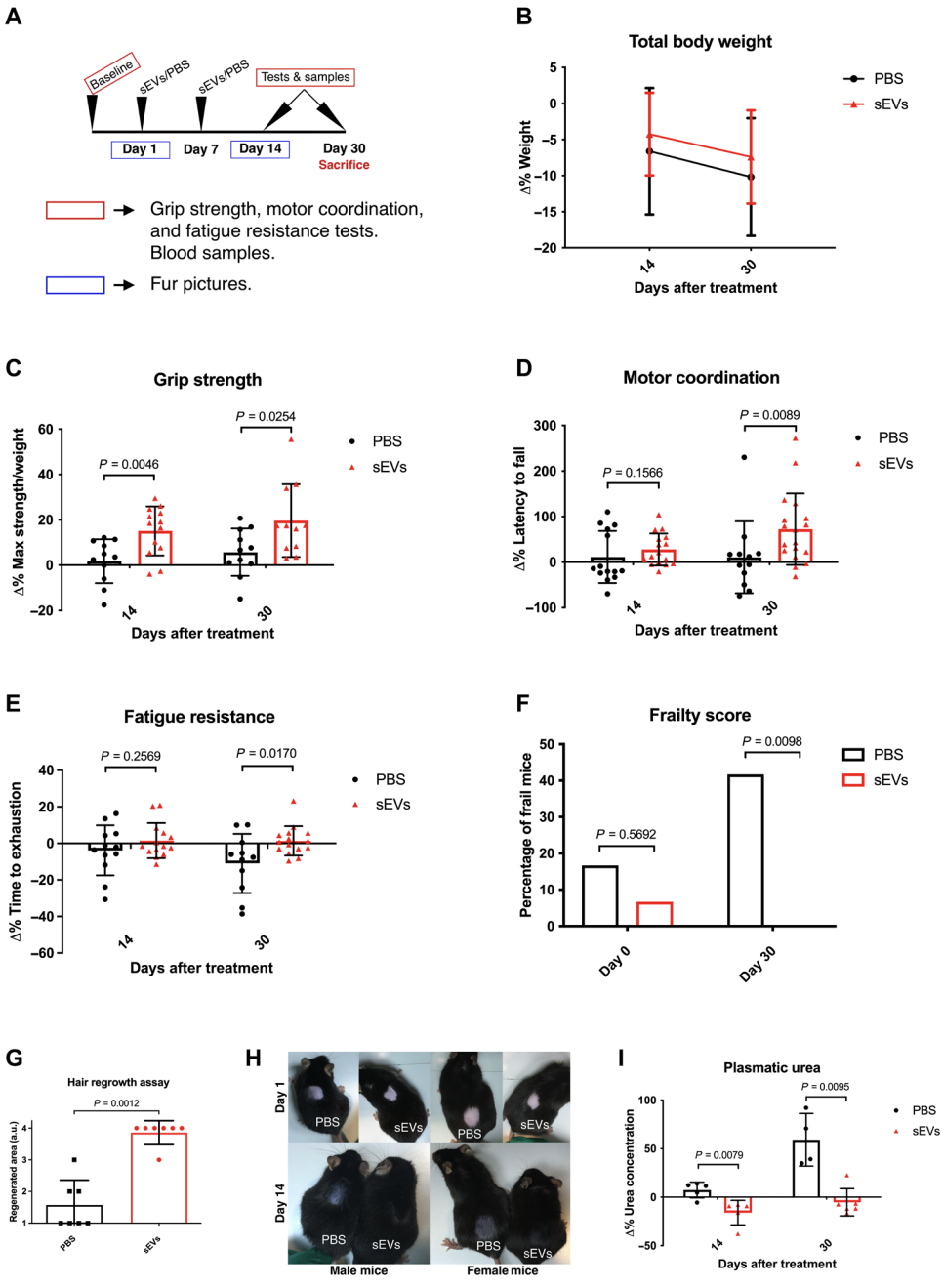

Fig. 2. ADSC-sEVs improve health span and prevent frailty in old mice. (**A**) Schematic representation of the experimental design. (**B**) Quantification of the change in total body weight; data are shown as the decrease in percentage from the baseline before treatment with sEVs/PBS. PBS: day 14, $n = 12$; day 30, $n = 12$; sEVs: day 14, $n = 14$; day 30, $n = 15$. (**C** to **E**) Quantification of the change in physical condition tests; data are shown as the change in percentage from baseline before treatment with sEVs/PBS. Grip strength: PBS: day 14, $n = 11$; day 30, $n = 11$; sEVs: day 14, $n = 13$; day 30, $n = 11$. Motor coordination: PBS: day 14, $n = 14$; day 30, $n = 12$; sEVs: day 14, $n = 16$; day 30, $n = 18$. Fatigue resistance: PBS: day 14, $n = 12$; day 30, $n = 11$; sEVs: day 14, $n = 14$; day 30, $n = 15$. (**F**) Quantification of the number of frail mice before and 30 days after treatment with sEVs/PBS, determined by a score based on the clinical phenotype of frailty. PBS: day 0, $n = 12$; day 30 $n = 12$; sEVs: day 0, $n = 15$; day 30, $n = 15$. (**G**) Quantification of the hair regrowth capacity of dorsal skin in old mice. PBS, $n = 7$; sEVs, $n = 7$. a.u., arbitrary units. (**H**) Representative image of hair regeneration in both male and female mice before and 14 days after treatment with sEVs/PBS. (**I**) Quantification of the changes in plasmatic urea; data are shown as the change in percentage from basal levels of urea in plasma before treatment with sEVs/PBS. PBS: day 14, $n = 5$; day 30, $n = 4$; sEVs: day 14, $n = 5$; day 30, $n = 6$. All data are shown as means ± SD.

fibrosis, we used Sirius red staining to measure collagen deposition. We noted a mild decrease in the ADSC-sEV–treated group, although no statistically significant differences were observed (Fig. 3, F and H).

These observations suggested that ADSC-sEVs may induce the proliferation of tubular cells as a means of regeneration, as these cells can repopulate renal tubules after damage (*39*). Using Ki67 as a proliferation marker, we looked for the presence of $Ki67^+$ cells in the

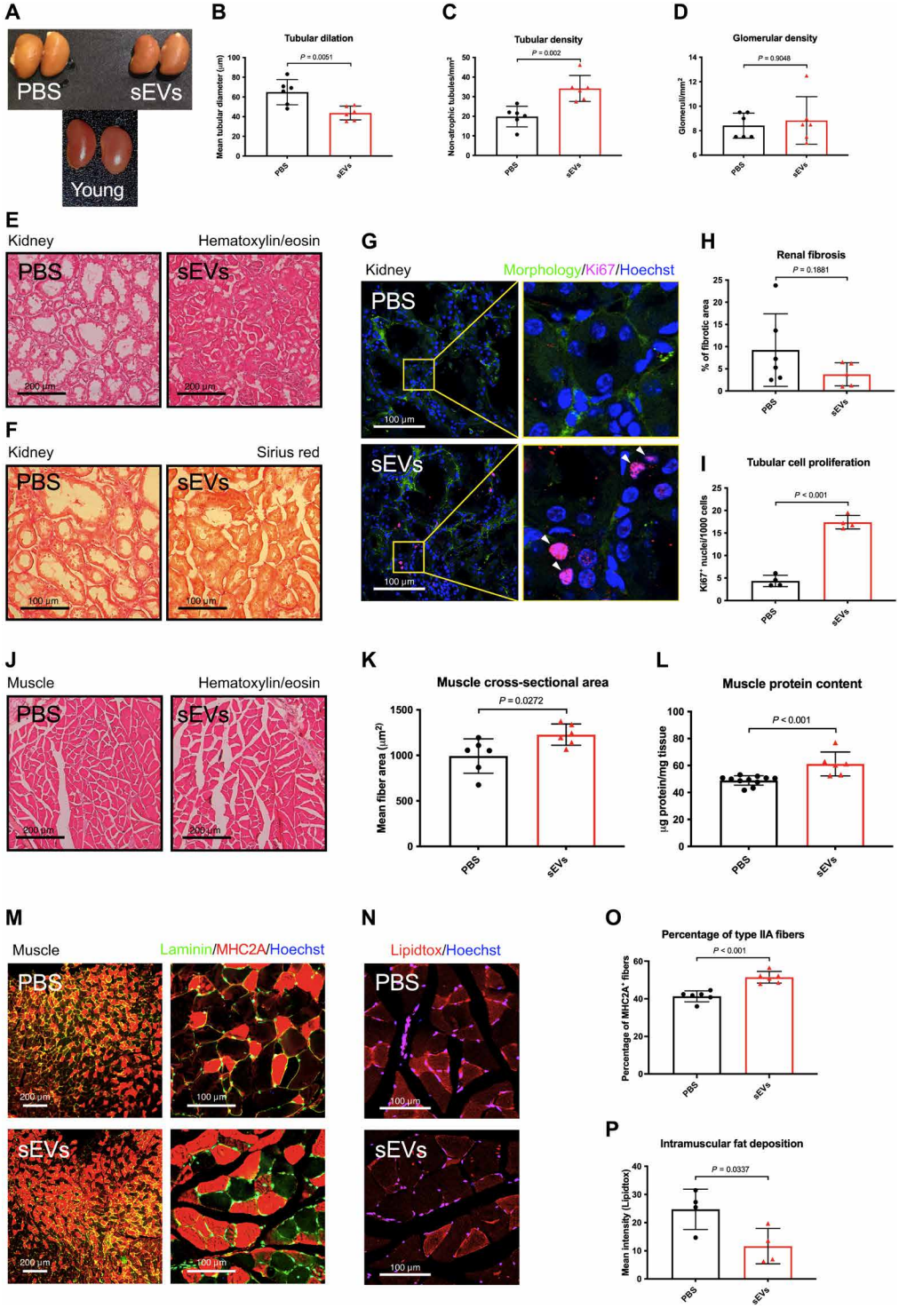

Fig. 3. ADSC-sEVs induce proregenerative effects on kidney and muscle of old mice. (**A**) Macroscopic image of kidneys isolated from old mice treated with PBS/sEVs. (**B** to **D**) Quantification of histological changes in the kidney (renal cortex) from old mice induced by sEVs. PBS, $n = 6$; sEVs, $n = 6$. (**E**) Hematoxylin and eosin representative images of the effects on the structure of the renal cortex of old mice. (**F**) Representative image of Sirius red staining of the renal cortex of old mice. (**G**) Representative immunofluorescence images showing Ki67$^+$ cells in the renal tubules of old mice. Morphology marker refers to background fluorescence to better depict tubular morphology. (**H**) Quantification of extracellular fibrosis by Sirius red staining. PBS, $n = 6$; sEVs, $n = 6$. (**I**) Quantification of Ki67$^+$ cells in the renal tubules of old mice. PBS, $n = 4$; sEVs, $n = 4$. (**J**) Hematoxylin and eosin representative images of gastrocnemius of old mice. (**K** and **L**) Quantification of the mean cross-sectional area (CSA) of muscle fibers and total protein content in the gastrocnemius of old mice. CSA: PBS, $n = 6$; sEVs, $n = 6$. Protein content: PBS, $n = 11$; sEVs, $n = 6$. (**M** and **N**) Representative immunofluorescence images of MHC2A and LipidTOX staining in gastrocnemius of old mice. (**O**) Quantification of the percentage of MHC2A$^+$ fibers in gastrocnemius of old mice. PBS, $n = 6$; sEVs, $n = 6$. (**P**) Quantification of LipidTOX staining intensity in gastrocnemius of old mice. PBS, $n = 4$; sEVs, $n = 4$. All data are shown as means ± SD.

cortex tubules of our mice. We found very low levels of proliferating cells in the control group; however, in the treated group, we identified a clear population of $Ki67^+$ tubular cells, indicating active proliferation of these cells in treated mice (Fig. 3, G and I).

Muscle loss of function and atrophy lead to a global dysfunction of the organism as it ages, as the musculoskeletal system is essential for the activities of daily life. The prevalence of sarcopenia (defined by a loss of muscle mass and function) increases with age (*40*). To investigate the effect of ADSC-sEVs on structural changes associated with aging in muscle tissue of old mice, we measured the cross-sectional area (CSA) of muscle fibers, which is a parameter related to muscle atrophy and loss of strength. We found an increase in the mean CSA with ADSC-sEV treatment, which was supported by a higher protein concentration in the muscles of ADSC-sEV–treated mice (Fig. 3, J to L). Sarcopenia is also accompanied by other cellular changes such as a loss of fast type II fibers and an increase in fat deposition (*41*). To test the effect of ADSC-sEVs on these parameters, we determined the percentage of type IIA fibers, finding a greater number of these fibers in old mice treated with ADSC-sEVs (Fig. 3, M and O). Using a fluorescent marker for lipids, we measured the degree of intramuscular fat deposition, and mice that received ADSC-sEVs showed a decrease in this parameter when compared to control mice (Fig. 3, N and P).

In summary, these results show that ADSC-sEVs induce pro-regenerative effects in the kidney and muscle, partially reverting structural changes associated with aging in these tissues.

ADSC-sEVs mitigate molecular traits associated with aging in the kidney and muscle and lower senescence in old mice and in an in vitro model

Multiple molecular traits contribute to the aging process (*2*). Here, we have studied the effect of ADSC-sEV treatment on several markers associated with aging: oxidative stress, senescence, inflammation, and telomere attrition. We obtained kidneys and muscle from old mice 30 days after treatment with ADSC-sEVs/PBS and studied how the treatment affected the presence of these markers. In the case of oxidative stress, we examined the levels of oxidation in two macromolecules, lipids, and proteins. We used malondialdehyde (MDA) as a marker of lipid peroxidation, and we observed lower levels of MDA in the muscle of mice treated with ADSC-sEVs, with no changes in the kidney (Fig. 4A). In protein oxidation levels, determined by carbonyl groups present in oxidized proteins, we found similar results as to those of MDA, with lower oxidation in the muscle of mice treated with ADSC-sEVs, and no changes in the kidney (Fig. 4B and fig. S1).

Telomere attrition and damage to telomeres are two of the most studied factors that lead to genomic instability and loss of proliferative capacity. Telomere shortening is observed in many species during normal aging, and excessively short telomeres are associated with multiple conditions characterized by a loss of regenerative capacity, such as pulmonary fibrosis, dyskeratosis congenita, and aplastic anemia (*42*). We explored the effect of ADSC-sEVs on telomere length and damage, as possible mediators of the observed effects in mice. For this purpose, we measured mean telomere length and DNA damage at the telomeres quantified as telomere dysfunction–induced foci (TIF). We did not find significant differences between both groups (Fig. 4, C and D), although we found that the muscle of treated mice showed slightly lower telomere damage than the nontreated ones.

Chronic inflammation is a condition closely related to aging and senescence; an increase in proinflammatory cytokines in several tissues has been linked to aging, frailty, and age-related diseases (*7*). Interleukin-6 (IL-6) and IL-1β are two of the most important factors of the senescence-associated secretory phenotype (SASP), so we measured the levels of these molecules in the kidney and the muscle of old mice, observing a decrease in IL-6 and IL-1β levels in both tissues from ADSC-sEV–treated mice (Fig. 4, E and F).

Senescent cells accumulate in aged tissues, having a detrimental effect on their function, as they are unable to enter the cell cycle. In addition, these cells act in a pleiotropic manner releasing several factors that make up the SASP, contributing to the development of age-associated diseases (*43*, *44*). We measured the loss of lamin B1 (LMNB1) and γH2AX as senescence markers (*45*) in muscle and kidney of old mice 30 days after treatment with ADSC-sEVs/PBS and noticed an important decrease in the number of senescent cells in both tissues in mice treated with ADSC-sEVs (Fig. 4, G to L).

Last, to test the effect of ADSC-sEVs on a more controlled environment, we developed an in vitro model of senescence in muscle progenitor cells. For this purpose, we used C2C12 mouse myoblasts and induced cellular senescence with palbociclib (5 μM). We treated the senescent cells with young ADSC-sEVs (5 μg/ml), and we measured senescence-associated β-galactosidase (SABG) as a senescence marker and annexin V as an apoptosis marker (see Fig. 4M for experimental design). We found that cells that received ADSC-sEVs showed a decrease in senescence and a decrease in the percentage of apoptotic cells (Fig. 4, N and O). As one of our main hypotheses was that ADSC-sEVs could be promoting the proliferation of specific cells in old individuals, we quantified $Ki67^+$ cells, showing an increase in cells treated with ADSC-sEVs (Fig. 4P). We also found a decrease in the release of proinflammatory molecules of the SASP (IL-6 and IL-1β) by the senescent cells treated with ADSC-sEVs (Fig. 4, Q and R). Last, we checked the effect of sEVs from other origins in senescent murine myoblasts (C2C12), using sEVs from murine fibroblasts (NIH3T3 cell line) and nonsenescent C2C12 myoblasts. We could not find any effect on the proportion of senescent cells using these sEVs (Fig. 4S), suggesting that sEVs from ADSCs contain specific factors that play a role in senescence. Overall, these findings prove that treatment with ADSC-sEVs can alleviate molecular and cellular traits of aging in the kidney and muscle of aged mice, inducing proliferation and a decrease in senescence, apoptosis, and SASP factors in an in vitro model of senescence.

Predicted epigenetic age is lower in tissues of old mice treated with ADSC-sEVs

We used multiple mouse clocks trained on different tissues to estimate the age of our treated and untreated animals. We grouped the clocks into two groups. The general clocks were trained across a wide spectrum of animals. The intervention group of clocks was trained on animals with age-affecting interventions. We used mixed-effects modeling to discern a trend across multiple clocks. In the kidney tissue samples, age estimates after the ADSC-sEV treatment were significantly lower for both general and intervention clocks ($P = 0.006$ and $P = 0.0002$, respectively). Similarly, in the liver tissue samples, both models showed a reduction in estimated age with the interventions group passing the statistical significance threshold ($P = 0.06$ and $P = 0.001$ for general and intervention clocks, respectively). Muscle and spleen tissues did not show a significant difference in age prediction between treated and control animal groups (Fig. 5A).

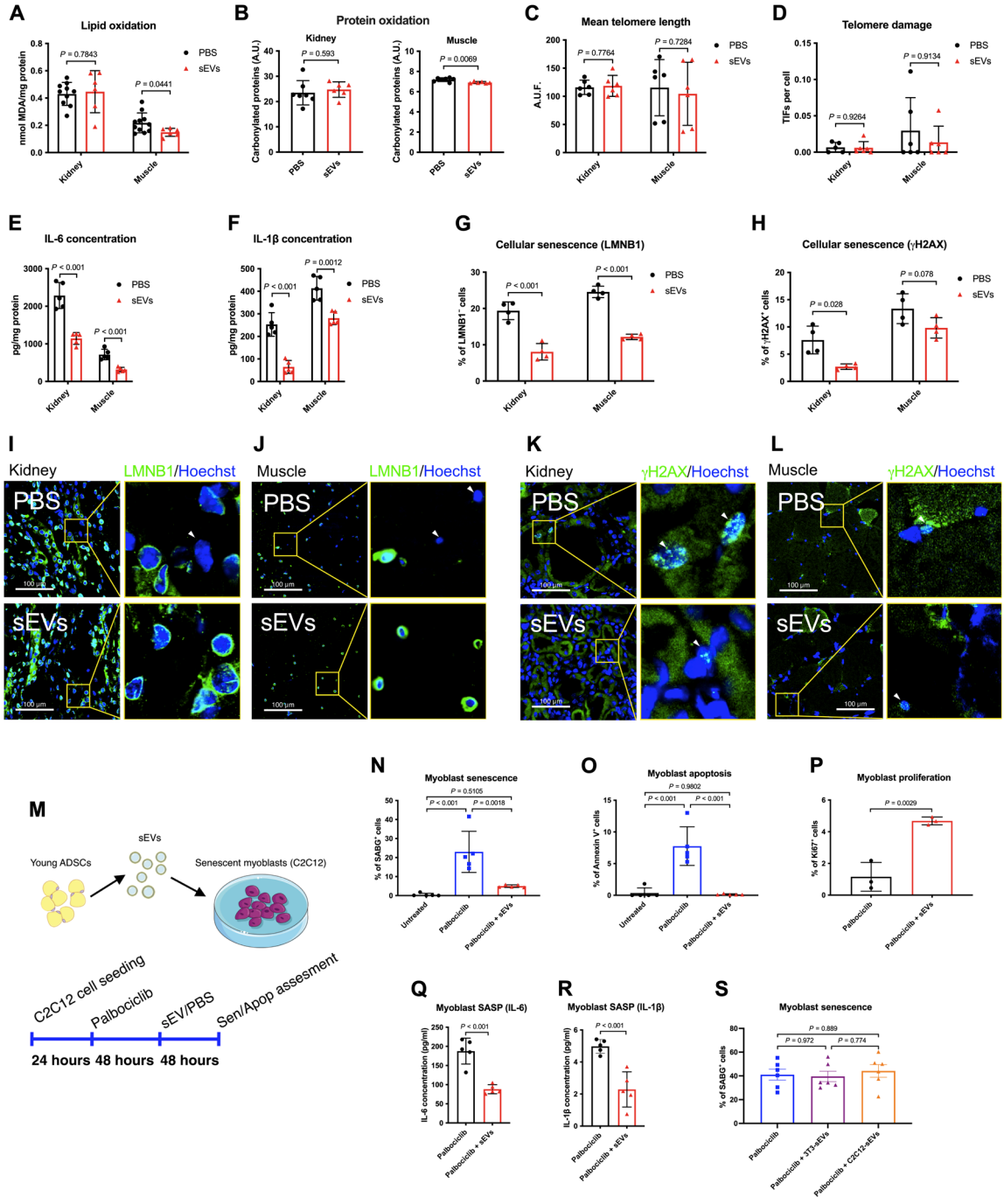

Fig. 4. sEVs from young ADSCs ameliorate molecular traits of aging in the kidney and muscle and lower senescence in old mice and in an in vitro model. (**A**) Quantification of MDA as a marker of lipid peroxidation in the kidney and muscle from old mice. PBS: kidney, $n = 10$; muscle, $n = 11$; sEVs: kidney, $n = 6$; muscle, $n = 6$. (**B**) Quantification of protein carbonylation as a marker of protein oxidation in the kidney and muscle of old mice. PBS: kidney, $n = 7$; muscle, $n = 7$; sEVs: kidney, $n = 6$; muscle $n = 6$. (**C**) Mean telomere length measured as arbitrary units of fluorescence (A.U.F.) in the kidney and muscle of old mice. PBS: kidney, $n = 6$; muscle, $n = 6$; sEVs: kidney, $n = 6$; muscle, $n = 6$. (**D**) Quantification of telomere dysfunction–induced foci (TIF) measured as number of telomeric probe and DNA damage marker 53BP1 colocalizing foci per cell by Immuno FISH in the kidney and muscle of old mice. PBS: kidney, $n = 5$; muscle, $n = 5$; sEVs: kidney, $n = 6$; muscle, $n = 6$. (**E** and **F**) Quantification of SASP factors IL-6 and IL-1β in the kidney and muscle of old mice. PBS: kidney, $n = 5$; muscle, $n = 5$; sEVs: kidney, $n = 5$; muscle, $n = 5$. (**G** to **L**) Quantification and representative immunofluorescence images of LMNB1 loss and γH2AX$^+$ cells in the kidney and gastrocnemius of old mice. PBS: kidney, $n = 4$; muscle, $n = 4$; sEVs: kidney, $n = 4$; muscle, $n = 4$. (**M**) Graphical representation of in vitro experiment with senescent murine myoblasts. (**N** and **O**) Assessment of senescence-associated β-galactosidase activity and annexin V by flow cytometry in senescent murine myoblasts. Untreated, $n = 5$; palbociclib, $n = 5$; palbociclib + sEVs, $n = 5$. All data are shown as means ± SD. (**P**) Quantification of Ki67$^+$ cells in senescent murine myoblasts. palbociclib, $n = 3$; palbociclib + sEVs, $n = 3$. (**Q** and **R**) Quantification of SASP factors IL-6 and IL-1β in senescent murine myoblasts. Palbocilib, $n = 5$; palbociclib + sEVs, $n = 5$. (**S**) Assessment of senescence-associated β-galactosidase activity by flow cytometry in senescent murine myoblasts. Palbociclib, $n = 6$; palbociclib + 3T3-sEVs, $n = 6$; palbociclib + C2C12-sEVs, $n = 6$. All data are shown as means ± SD.

Linear regression analysis revealed abundant differentially modified loci in all tissues [n = 5.546, 36.163, 7.247, and 11.092 in the spleen, liver, kidney, and muscle, respectively; robust linear regression, false discovery rate (FDR), $q < 0.05$]. We assigned each locus the nearest gene name and performed gene set enrichment analysis using g:profiler (*46*). Although affected pathways were different across tissues, we observed developmental, neuronal, and synaptic pathways similarly affected in all tissues (Fig. 5, B to E).

ADSC-sEVs induce a change in the metabolome of old mice to a youth-like pattern

We quantified 72 metabolites in blood plasma samples from seven PBS-treated and six ADSC-sEV–treated old mice from four control young mice. Fourteen of these metabolites show statistically significant differences between ADSC-sEV–treated and untreated old animals (Fig. 6, A and B, and table S5). Most of the significant metabolites were amino acids including essential (isoleucine, tryptophan, threonine, and valine) and nonessential (aspartate, arginine, tyrosine, glycine, and proline). Some of these amino acids have been previously associated with metabolic health like the branched-chain amino acids isoleucine and valine (*47*) as well as tryptophan (*48*). Lactate is formed by the anaerobic glycolysis in most mammalian tissues. Together with acetate, it is also a product of fermentation of fructans and other prebiotics by gut microbiota (*49*). They are further processed into butyrate and other short-chain fatty acids by some strains of *bifidobacteria* and *lactobacilli*, which suggest some impact of ADSC-sEV treatment in gut microbiota ecosystems. The heatmap of these metabolites shows a clustering trend among groups (Fig. 6A) and some resemblance between ADSC-sEV–treated old mice and young mice (Fig. 6B), i.e., red dots (old-sEV mice) differ from black ones (old-PBS mice) but coincide with blue dots (young mice).

To further explore this resemblance, we built a partial least-squares discriminant analysis (PLS-DA) model with all the metabolites for discriminating between old and young untreated animals and projected into this model the samples from ADSC-sEV–treated animals. The score plot of all the samples in this model shows the same resemblance between old treated and young animals along the latent variable 2 (LV2) dimension, suggesting that ADSC-sEV treatment partially ameliorates the impact of aging on the metabolome (Fig. 6C). Thirteen of the fourteen metabolites significantly associated with treatment also show a PLS-DA VIP (variable importance in projection) score higher than 1, which confirms interactions between age-related metabolomic changes and ADSC-sEV treatment (Fig. 6D).

Last, we performed a metabolite set enrichment analysis (MSEA) concerning the Small Molecule Pathway Database (SMPDB) for mammal's metabolism to gain biological insight into the metabolome changes induced by the ADSC-sEV treatment. The only three metabolite clusters enriched in our data with statistical significance were the arginine and proline metabolism cluster, the glycine and serine metabolism cluster, and the aspartate metabolism cluster with five, four, and three hits, respectively (Fig. 6E). These three clusters, especially the arginine and proline clusters, have been previously associated with cardiometabolic health in humans (*50*). Besides the well-known role of arginine as urea or nitric oxide precursor, arginine is also a precursor of proline and is relevant for collagen biosynthesis (*51*). Proline and glycine, the two most abundant amino acids in collagen accounting for 23% of the molecule, are also represented in the first three clusters of our MSEA suggesting some involvement of collagen metabolism in the potential beneficial effects of ADSC-sEV treatment.

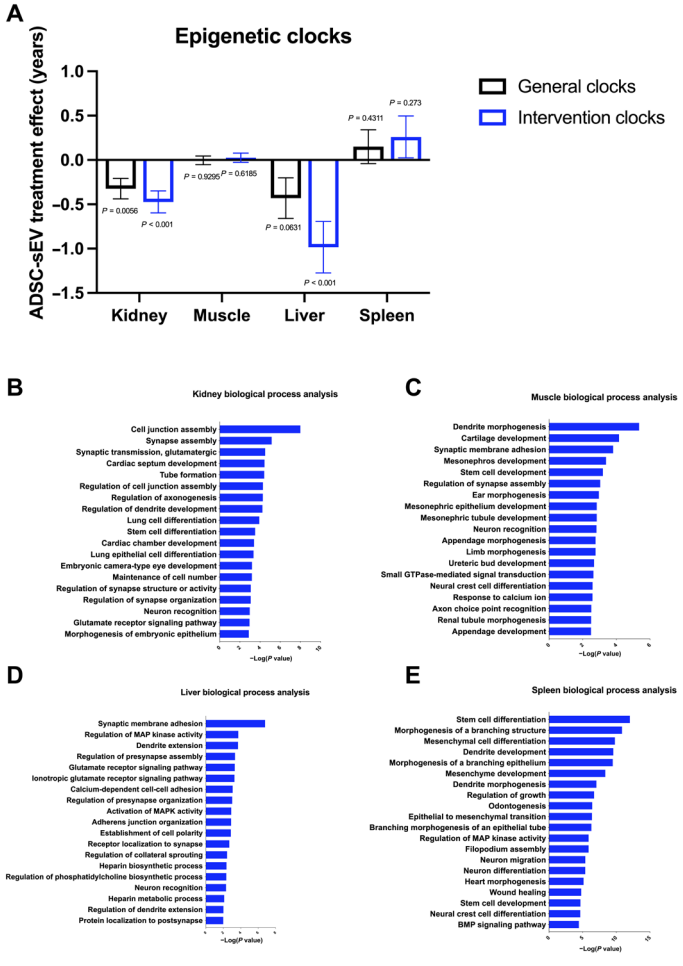

Fig. 5. ADSC-sEVs decrease the epigenetic age of several tissues in old mice. (**A**) ADSC-sEV treatment effect on epigenetic age estimation mixed-effects modeling across several tissues. (**B** to **E**) Biological process enrichment analysis of differentially methylated cytosines in ADSC-sEV–treated tissues (liver, muscle, kidney, and spleen, respectively). PBS, $n = 6$; ADSC-sEVs, $n = 6$. All data are shown as means ± SD. BMP, bone morphogenetic protein; GTPase, guanosine triphosphatase; MAP, mitogen-activated protein; MAPK, MAP kinase.

Analysis of sEV miRNA content reveals that up-regulated miRNAs in young ADSC-sEVs govern tissue development and regeneration pathways

Motivated by these results, we attempted to investigate candidate factors present in ADSC-sEVs that could be responsible for the beneficial effects in old mice. miRNAs are an important fraction of several types of EV content and can regulate transcription in several tissues (*52*). Here, we used miRNA profiling (Affymetrix GeneChip miRNA 4.0 Array) to study miRNAs contained in sEVs. We obtained sEVs from three different conditions: supernatant of young and old ADSCs, and plasma from aged mice. In the analysis, miRNAs with a twofold increase or decrease in expression and a P value < 0.01 were defined as significantly different. Principal components analysis (PCA) showed three differentiated groups of samples (Fig. 7A). Analysis of 3196 miRNAs in sEVs from young ADSC cultures

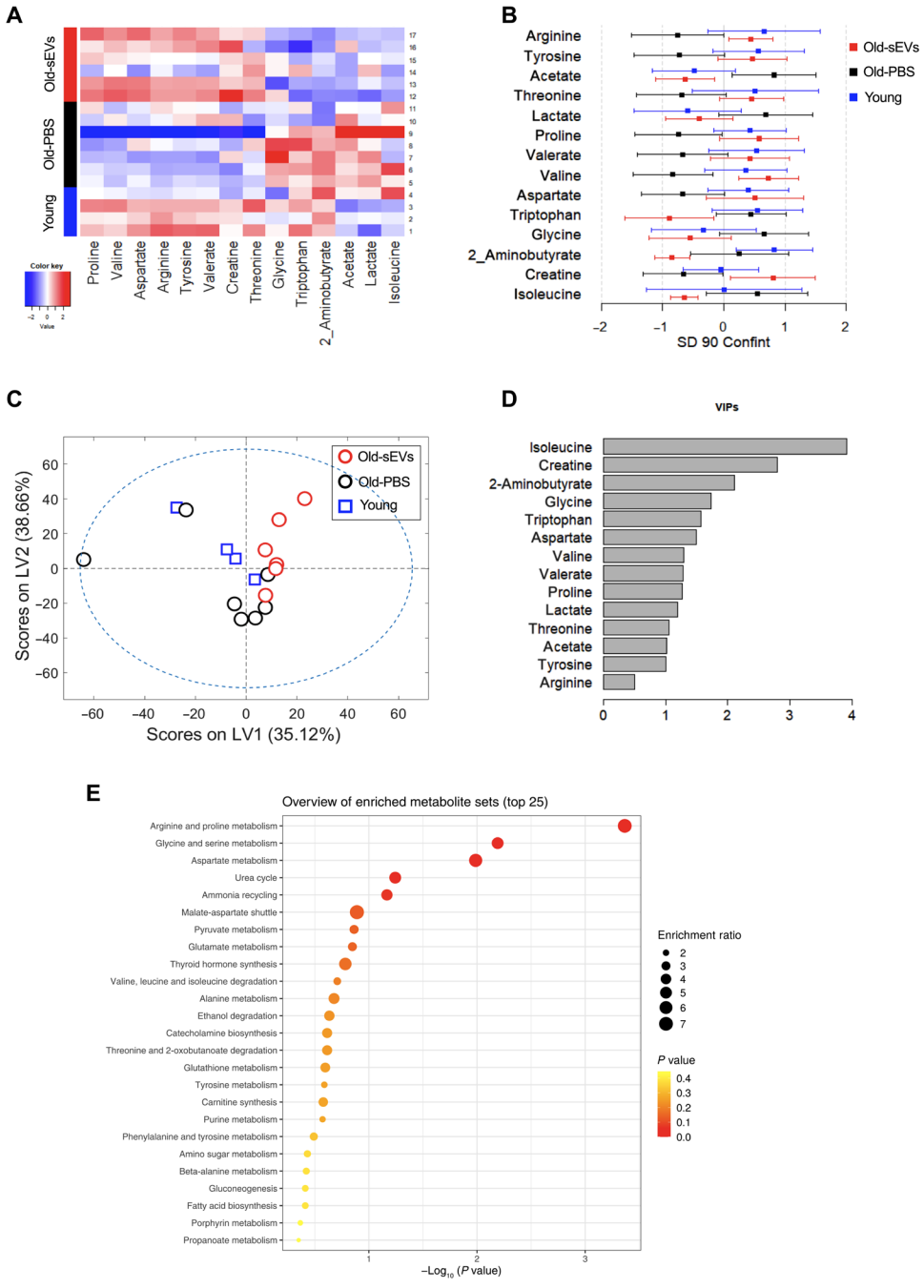

Fig. 6. The metabolome of ADSC-sEV–treated mice resembles that of young animals. (**A**) Heatmap of metabolite *z* scores with statistically significant differences between old-PBS (black bar samples) and old-sEV (red bar samples) mice compared with young untreated mice (blue bar samples). (**B**) Mean and 90% confidence intervals for *z* scores in SD units for the same metabolites that (A) in old-PBS (black), old-sEVs (red), and young untreated (blue) mice. (**C**) Score plot for a metabolome partial least-squares discriminant analysis (PLS-DA) model (72 metabolites) for discrimination between young (blue squares) and old-PBS (black circles) mice. Old mice treated with sEVs (red circles) are projected in the score plot. (**D**) Variable importance in projection (VIP) scores in the metabolome PLS-DA model of (C) for those metabolites significantly associated with treatment. (**E**) Enrichment ratio (size of the circle) and *P* values (color of the circle) for the 25 most enriched metabolite sets from a metabolite set enrichment analysis (MSEA) on the Small Molecule Pathway Database (SMPDB) and our 14 significant metabolites. The *n* used for all metabolomic analyses was young mice, $n = 4$; old-PBS mice, $n = 6$; and old-sEV mice, $n = 6$.

showed several differentially expressed miRNAs when compared to sEVs from old ADSC cultures (9 up-regulated and 1 down-regulated) and from plasma of aged mice (25 up-regulated and 4 down-regulated; Fig. 7, B to D). In all comparisons, sEVs from young ADSCs showed an increased miRNA expression profile, in accordance with previous findings that showed a deregulated miRNA biosynthesis with aging, especially in the adipose tissue (*53*–*55*). These miRNAs are shown in tables S6 to S8.

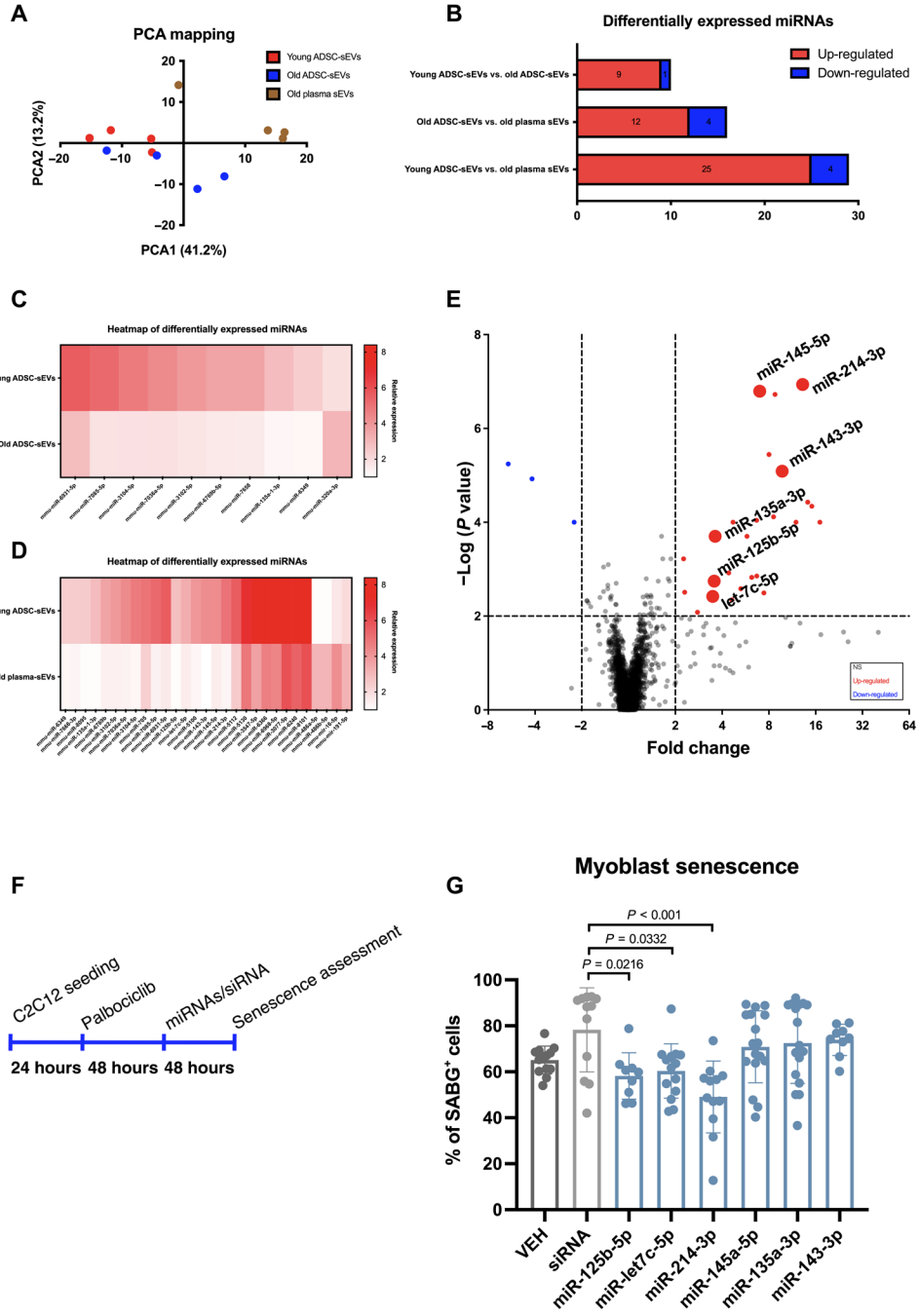

Fig. 7. Tissue development and regeneration are major targets of miRNAs enriched in young ADSC-sEVs, with an effect on senescence in vitro. (**A**) PCA of miRNA profiling in sEVs from young ADSCs, old ADSCs, and plasma of aged mice. Old plasma, $n = 4$; old ADSC-sEVs, $n = 4$; and young ADSC-sEVs, $n = 4$. (**B**) Summary of differentially expressed miRNAs under the three conditions. (**C**) Heatmap of differentially expressed miRNAs in sEVs from young and old ADSCs. (**D**) Heatmap of differentially expressed miRNAs in sEVs from young ADSCs and plasma of aged mice. (**E**) Volcano plot showing the different miRNA expression between plasma of aged mice and young ADSC-sEVs. NS, not significant. (**F** and **G**) Assessment of senescence-associated β-galactosidase activity by flow cytometry in senescent murine myoblasts treated with miRNA mimics. Vehicle (VEH), $n = 13$; small interfering RNA control, $n = 13$; miR-125b-5p, $n = 9$; miR-let7c-5p, $n = 17$; miR-214-3p, $n = 15$; miR-145a-5p, $n = 17$; miR-135a-3p, $n = 17$; miR-143-3p, $n = 9$.

As we injected the young ADSC-sEVs into the blood of old mice, we reasoned that miRNAs up-regulated in the young ADSC-sEVs and with low levels in plasmatic sEVs from aged mice may be, at least in part, responsible for the beneficial effects of ADSC-sEVs. Thereafter, we explored the predicted mRNA targets for the up-regulated 25 miRNAs and their role in biological processes and molecular pathways. However, as the number of predicted targets was too high for further analysis, we outlined six miRNAs as plausible biologically relevant, i.e., that can be considered relevant because these miRNAs (highlighted in red in Fig. 7E) are the ones that share their

nucleotide sequence among several species, including humans, as many features of the aging process are highly conserved across species (*56*).

Together, these six miRNAs were predicted to target 5.379 genes with very high stringency (top 1% in confidence, present in at least five databases as curated by miRDIP). The target gene dataset was then introduced in PANTHER to study overrepresented biological processes and pathways (*57*). A great number of genes targeted by our miRNAs were involved in cell proliferation, tissue development, growth, and regeneration (fig. S2). Regarding molecular pathways, these miRNAs regulated important pathways related to tissue regeneration, fibrosis, and inflammation, such as angiogenesis, Wnt signaling, platelet-derived growth factor, fibroblast growth factor, transforming growth factor–β, IL, and interferon-γ signaling. They targeted critical pathways in the aging process, including apoptosis, p53 signaling, p38 mitogen-activated protein kinase, oxidative stress response, and insulin/IGF pathway (fig. S2). In conclusion, predicted targets of the selected miRNAs up-regulated in young ADSC-sEVs compared with plasma sEVs of old mice are probably involved in several relevant processes and pathways affected during aging.

To explore the role of these miRNAs in a biological process related to aging, we treated senescent murine myoblasts with miRNA mimics (Fig. 7F). We found that three of our selected miRNAs—miR-125b-5p, miR-let7c-5p, and miR-214-3p—were able to lower senescence in vitro (Fig. 7G), indicating a plausible role of miRNAs contained in sEVs as modulators of this process.

DISCUSSION

Aging is the largest risk factor for most diseases that affect people at the late stages of their lives. Our understanding of the aging process has grown greatly in the past decades, providing us with several biochemical changes that are considered drivers of this process; oxidative stress, telomere attrition, and cellular senescence are some of these biological processes that are proposed as drivers of age-related morbidities (*2*). An altered intercellular communication is one of the ultimate culprits of tissue and organismal aging, and several players of intercellular communication have been proposed as possible antiaging factors in parabiosis experiments (*10*, *11*, *58*). sEVs could be one important fraction of the factors present in young environments that can have a beneficial effect on aged individuals. sEVs from MSCs have a regenerative capacity themselves, can help tissue to regenerate after damage, and are potential cell-free therapeutic agents (*59*). Nicotinamide phosphoribosyl transferase was shown to be present within plasmatic EVs, and these EVs were able to ameliorate several parameters affected by aging and increased the life span of old mice (*31*). Similarly, sEVs have been described as carriers of glutathione *S*-transferase activity, which can ameliorate senescence and oxidative stress–related damage in old mice (*29*). More recently, sEVs from MSCs were able to extend life span in a transgenic mouse model of accelerated aging and mitigated several senescence-associated markers in vivo and vitro (*60*).

Given this background, the effect of sEVs from young MSCs on the function of tissues affected by aging in physiologically aged mice remained to be elucidated. In the present work, we have shown that young ADSC-sEVs have great potential as antiaging factors, as old mice injected with these sEVs showed an improvement in several functions affected by aging, such as physical condition, fur regeneration, and renal function, as well as a reduction of frailty. As we based our determination of renal function on the concentration of urea, it is important to mention that this might be a result of a decreased catabolic rate in skeletal muscle, as we have observed an increase in CSA and protein content in muscle of ADSC-sEV–treated mice. The effect of ADSC-sEVs seems to be finite, as we observed in a more long-term experiment that the effect on the functionality of old mice was lost 2 months after treatment with ADSC-sEVs. Moreover, sEVs induced structural changes in tissues from old mice, exhibiting a potent proregenerative effect in these tissues, which is in accordance with previous results that proposed sEVs as a regenerative tool (*29*). We observed a reduction of senescence in tissues and in vitro when sEVs were introduced; however, the mechanism of action remains unclear, as we did not find senolytic activity. They may probably act as senomorphics, molecules that suppress the senescent phenotype without the specific induction of apoptosis in senescent cells, probably through the inhibition of the SASP, as has been suggested recently (*60*). We found a reduced level of IL-6 and IL-1β, two of the main SASP factors, in the tissues from ADSC-sEV–treated mice and in the in vitro model of senescence. IL-6 is a key factor of the SASP, but its role in muscle physiology and function goes beyond inflammation, as it is an important myokine that stimulates its expression with exercise (*61*); thus, the modulation of this factor may be key in the effects observed in the muscle of treated mice. All these effects found in tissues of ADSC-sEV–treated mice were accompanied by a decrease in the epigenetic age estimation from epigenetic clocks, which are recognized as a feasible estimation of biological age (*62*). Some of the most studied interventions in aging, such as caloric restriction or rapamycin treatment, have demonstrated a strong impact on predicted epigenetic age (*63*–*65*). To our knowledge, this study is the first to show that intervention with sEVs can decrease epigenetic age in an old organism.

sEVs induced effects not only in individual tissues but also in the whole metabolome of old mice, which turned to a youth-like pattern, indicating that the effects observed are probably part of a pleiotropic effect on the organism. Now as it is time to continue investigating the molecules that are included in sEVs, we have explored miRNAs contained in young ADSC-sEVs and found that they are involved in several processes and pathways affected by aging, thus proposing miRNAs as possible mediators of the effects shown in mice. Taking into account our results and other preliminary studies, miR-214-3p may play a role in senescence (*66*, *67*). It is important to point out the debate on the relevance of miRNAs in the function of EVs, as recent studies have shown low levels of miRNAs in EVs, along with a limited delivery into target cells (*68*, *69*). More studies are needed to identify factors derived from stem cells that can assist tissue function and regeneration, as they could have an enormous impact on age-related pathologies, such as frailty or renal failure.

MATERIALS AND METHODS

Animal model

This study was performed in strict accordance with all applicable federal and institutional policies. The protocol was approved by the University of Valencia Animal Ethics Committee following European Union (EU) regulations on animal research (identification numbers A1490612630929 and A1508582840889). All the mice used in this study were of a C57BL/6J background. Aged mice used were treated at 20 to 24 months of age. Both sexes were used throughout the study. Where feasible, littermates of the same sex were used. The sample

size needed was calculated using G*Power. These were randomly assigned to experimental groups. All experiments were addressed blindly. The experimental procedure was replicated throughout the study, as mice from six batches (sEVs versus PBS) were used. After mice were euthanized, plasma and organs were obtained and stored at −80°C. For all the experiments conducted in the kidney and gastrocnemius, we used organs obtained from mice 30 days after treatment with sEVs/PBS. The mean age of mice that received sEVs was 21,925 months and that of mice that received PBS was 21,975 months. For the mice that were euthanized on day 30 to obtain tissues for the analysis, the mean age was 22.15 months for the sEV group and 21.75 months for the PBS group.

Stem cell culture

Mice at 3 to 6 months of age from both sexes were used to obtain MSCs from both inguinal fat pads with the previously described protocol (*70*). All cells were used in passages 2 and 3 for the experiments. The culture medium used for the expansion and maintenance of the cells was high-glucose Dulbecco's modified Eagle's medium (DMEM) with 10% FBS and 1% penicillin/streptomycin (P/S). Cells were maintained at 37°C, 5% CO_2, and 3% O_2 (Whitley H35 HEPA Hypoxystation).

ADSC characterization

For the characterization of ADSCs, we analyzed the presence of typical MSCs markers (CD29, CD44, CD90, and CD105) by flow cytometry; CD45 and CD31 were used as negative controls. When cells reached 80% confluency, they were trypsinized and resuspended in fluorescence-activated cell sorting (FACS) buffer (10% FBS and 1% sodium azide in PBS). A total of 100,000 cells were used for each condition; they were stained with antibody (1 μg/μl) and incubated for 30 min at 4°C. All antibodies were acquired from BioLegend: CD29 R-phycoerythrin/Cyanine7 (PE/Cy7), 10222; CD31 PE, 102507; CD44 Alexa Fluor 488, 103015; CD45 PE, 103106; CD90 fluorescein isothiocyanate (FITC), 140303; and CD105 allophycocyanin (APC), 120413.

ADSCs isolated from inguinal fat pads of young mice showed a strong expression of MSCs markers; cells were positive (>80%) for CD29, CD44, CD90, and CD105 and negative for hematopoietic (CD45) and endothelial (CD31) markers (fig. S3).

ADSC-derived sEV isolation

ADSCs at passages 2 and 3 were expanded until they reached 80% confluency; at that moment, medium was changed to high-glucose DMEM with 2% exosome-depleted FBS (Gibco, A2720803) and 1% P/S. After 48 hours, conditioned medium was collected, and sEVs were isolated by differential ultracentrifugation. Medium was centrifuged at 2000*g* for 10 min and then at 20,000*g* for 30 min to remove whole cells, cell debris, and bigger EVs. The supernatant was then ultracentrifuged at 100,000*g* for 70 min. Pelleted vesicles were suspended in PBS, ultracentrifuged again at 100,000*g* for 70 min for washing, resuspended in PBS, and prepared for treatment, NTA, electron microscopy, or flow cytometry analysis. For the non-EV fraction injections, we used 20 μg of protein from conditioned cell culture medium obtained after the first ultracentrifugation step.

ADSC-derived sEV NTA

The size distribution of vesicles was determined by NTA in a NanoSight LM10 (Malvern Instrument Ltd., Malvern, UK), using a 405-nm laser and a scientific complementary metal-oxide semiconductor camera. Data were analyzed with the NTA software version 3.3. (Dev Build 3.3.104), with Min track Length, Max Jump Distance, and Blur set to auto, and the detection threshold was set to 5. The camera level was set to 15 and five readings of 30 s at 30 frames per second. Images were taken with manual monitoring of temperature. Samples were diluted at 1:200 with filtered PBS to reach the concentration (20 to 120 particles per frame) recommended by the manufacturer.

ADSC-derived sEV immunoblotting

sEVs were resuspended and lysed in tris/SDS/glycerol buffer, protein concentration was determined using the Lowry method, and 20 μg of proteins were separated on SDS polyacrylamide gels and transferred onto nitrocellulose membranes; as a control for the sEV immunoblotting, we used FBS used in the isolation of sEVs (Gibco). The membranes were blocked with 3% bovine serum albumin (BSA) in tris-buffered saline with 0.05% Tween 20 (TBS-t) for 60 min at room temperature (RT) and incubated overnight at 4°C with anti-TSG101 antibody (Proteintech, 28283-1-AP; 1:1000 dilution) or BSA antibody (Proteintech, 66201-1-Ig). Following three washes (10 min) with TBS-t, membranes were incubated with secondary antibody (anti-rabbit; Cell Signaling Technology, 70745; 1:2000 dilution; anti-mouse, BioLegend, 401215; 1:1000 dilution) for 60 min at RT. Following three washes with TBS-t, membranes were developed with Luminol (Sigma-Aldrich) in the ImageQuant LAS4000 system. Images were processed in ImageJ.

ADSC-derived sEV flow cytometry

For flow cytometry analysis, pellets obtained from 10 ml of medium were resuspended in 100 μl of PBS. sEVs were stained with APC anti-CD63 (4 μg/ml; BioLegend, 143905) for 30 min at 4°C in darkness. After incubation, positive events were read by FACSVerse flow cytometry. One unstained sample of sEVs and one sample with the antibody at 4 μg/ml in PBS were used as negative controls. Calibration of the cytometer was assessed using fluorescent particles of standardized size (Nano Fluorescent Particle Size Standard Kit, Spherotech).

ADSC-derived sEV electron microscopy

The isolated sEVs were fixed in 2% paraformaldehyde (PFA)–0.1 M PBS for 30 min. Glow discharge technique (30 s, 7.2 V, using a Bal-Tec MED 020 Coating System) was applied over carbon-coated copper grids, and immediately, these grids were placed on top of sample drops for 15 min. Then, the grids with adherent sEVs were washed in a 0.1 M PBS drop, and additional fixation in 1% glutaraldehyde was performed for 5 min. After washing properly in distilled water, the grids were contrasted with 1% uranyl acetate and embedded in methylcellulose. Excess fluid was removed and allowed to dry before examination with a transmission electron microscope FEI Tecnai G2 Spirit (Thermo Fisher Scientific, OR, USA). All images were acquired using a digital camera Morada (EMSIS GmbH, Münster, Germany).

Immunogold labeling of sEVs

In brief, 8 μl of isolated sEVs were fixed in 2% PFA–0.1 M PBS for 30 min, and carbon-coated nickel grids were placed on top of these sEV drops for 15 min. Then, the grids with adherent sEVs were washed in 0.1 M PBS and blocked in 0.1 M glycine and 0.3% BSA for 10 min. The grids were incubated with anti-CD63 (MBL, D263-3) primary antibody (1:100 dilution) for 1 hour. After another blocking step for 10 min, the grids were incubated in Gold 6nm–conjugated goat anti-rat (Abcam, ab105300) secondary antibody (1:1000 dilution)

for 1 hour. Last, after washing, a standard negative staining procedure was made and observed under a transmission electron microscope as previously described.

In vivo tracking of sEVs with PKH26 staining

For the in vivo tracking of sEVs, we isolated sEVs from the conditioned medium of young ADSCs and labeled them after the first ultracentrifuge with 5 μM PKH26 (Sigma-Aldrich, MINI26-1KT), after that, sEVs were resuspended in PBS and washed with another ultracentrifuge. Twenty micrograms of PKH26-labeled sEVs were injected in old mice (18 months), mice were euthanized 24 hours later, and kidney and gastrocnemius were obtained and fixed with 2% PFA for 24 hours. Forty-micrometer slices were mounted and stained with Hoechst (Invitrogen) 1:1000 for 30 min at RT. Coverslips were mounted with an aqueous mounting medium and sealed with nail polish. Images were acquired with Olympus FV1000 confocal laser scanning biological microscope. Images were processed in ImageJ, all levels were adjusted equally, and the ratios were not altered.

Treatment preparation

sEVs isolated from the conditioned medium were kept at 4°C and used for treatment within 24 hours. To determine the dose of sEVs, we performed protein quantification with the Lowry method of the sEV samples. Each dose consisted of either 20 μg of sEVs' protein or PBS as a control in a total volume of 100 μl. Mice were intravenously injected with the preparation in the tail vein.

Physical condition tests

The Grip Strength Meter (Panlab, Harvard Apparatus) was used in assessing neuromuscular function by sensing the peak amount of force that the mice applied in grasping specially designed pull bar assemblies. Peak force was automatically registered in gram-force by the apparatus. Data were recorded, and two additional trials were immediately given. Maximum force was normalized to the weight of the mouse. Animals were submitted to a graded intensity treadmill test (Treadmill Control LE 8710 Panlab, Harvard Apparatus) to determine their endurance (running time) and running speed along with the study. After a warm-up period, the treadmill band velocity was increased until the animals were unable to run further. The initial bout of 4 min at 10 cm/s was followed by consecutive 4 cm/s increments every 2 min. Exhaustion was reached when a mouse remained on the shock grid for 5 s rather than running. Motor coordination was assessed with a Rota Rod (Panlab, Harvard Apparatus no. 76-0772), consisting of a 3-cm-wide wheel that rotates with an increasing speed. Time to fall was recorded for each mouse, with a total of three trials. To assess frailty quantitatively, we used a score based on the clinical phenotype of frailty developed in our group (*34*), mice with three or more criteria were classified as frail. Criteria used are as follows: loss of 5% of body weight, time to fall in Rota Rod under percentile 20 (p20), time to exhaustion in a treadmill under p20, maximum speed reached in a treadmill under p20, and normalized grip strength under p20.

Hair regrowth assay

On day 1, dorsal hair was removed by plucking from a square of approximately 1 cm by 1 cm. Hair regrowth was scored 2 weeks later, based on digital photographs and a semiquantitative assessment, using an arbitrary scale from one to four (where four represents complete hair regeneration). Scoring was performed blindly by two independent investigators.

Plasmatic urea value measurement

One hundred microliters of whole blood was obtained from the saphenous vein of each mouse just before treatment; after that, whole blood was obtained on days 14, 30, and 60. Whole-blood samples were collected in a microvette with EDTA for plasma separation and spun for 15 min at 1500*g*. The clear supernatant was transferred into regular 1.5-ml tubes, snap-frozen in liquid N_2, and stored at −80°C. Urea concentration was measured using a QuantiChrom urea assay kit (Gentaur). The samples were incubated in a 200-μl reaction mix for 20 min at RT before absorbance was measured at 520 nm (Molecular Devices SPECTRAmax Plus 384). All samples were assayed in duplicate.

Histological analysis

Kidneys and gastrocnemius were fixed in 4% PFA for 48 hours and then cryoprotected with 30% sucrose in PBS; 10-μm slices were obtained in a cryostat for histological staining and immunofluorescence. Slices were stained with hematoxylin (Sigma-Aldrich, MHS32) and eosin (Sigma-Aldrich, E4009) or with Sirius red (Sigma-Aldrich, 365548), mounted, and sealed for further morphometric analysis. Images were obtained using an optical microscope (Leica), and three images from different areas of each slice were obtained. All levels were adjusted equally, the ratios were not altered, and morphometric analysis of kidney and muscle sections was performed with ImageJ.

Immunofluorescence

Ten-micrometer tissue slices were mounted in slides and heated for 30 min in tris-EDTA buffer (pH 10) for antigen retrieval and permeabilized with 1% Triton X-100 in PBS (Ki-67, γH2AX) or 1% Tween 20 in PBS (MHC2A, Laminin, LMNB1), depending on the antibody. Sections were blocked with 10% normal goat serum (Invitrogen) in PBS with 0.05% Tween 20 (PBS-t) and incubated with primary antibody overnight at 4°C. After incubation with primary antibody, sections were washed three times with PBS-t and incubated with secondary antibody for 2 hours at RT, washes were repeated, and tissues were counterstained with Hoechst (Invitrogen; 1:1000 dilution) for 30 min at RT. Coverslips were mounted with an aqueous mounting medium and sealed with nail polish.

Images were acquired with Olympus FV1000 confocal laser scanning biological microscope. Images were processed in ImageJ, all levels were adjusted equally, the ratios were not altered, and three images from different areas of each slice were obtained.

Ki67 staining antibodies: anti-Ki67 (Thermo Fisher Scientific, PA5-19462; 1:1000 dilution) and Alexa Fluor 647 anti-rabbit (Abcam, ab150079; 1:1000 dilution); a minimum of 1000 nuclei were analyzed per sample. MHC2A staining antibodies: anti-MHC2A (DSHB, 2F7; 0.5 μg/ml) and Alexa Fluor 647 anti-mouse (Cell Signaling Technology, 4410; 1:1000 dilution); a minimum of 200 fibers were analyzed per sample. Laminin staining antibodies: anti-laminin (Thermo Fisher Scientific, PA1-16730; 1:500 dilution) and Alexa Fluor 488 anti-rabbit (Abcam, ab150079; 1:2000 dilution); a minimum of 200 fibers were analyzed per sample. LMNB1 staining antibodies: anti-LMNB1 (Proteintech, 12987-1-AP; 1:50 dilution) and Alexa Fluor 488 anti-rabbit (Abcam, ab150079; 1:2000 dilution); a minimum of 400 nuclei for kidney and 100 nuclei for muscle were analyzed per sample. γH2AX staining antibodies: anti- γH2AX (Cell Signaling Technology, 9718S; 1:1000 dilution) and Alexa Fluor 488 anti-rabbit (Abcam, ab150079; 1:2000 dilution); a minimum of 400 nuclei for kidney and 140 nuclei for muscle were analyzed per sample. For the intramuscular fat staining, slices were not heated for antigen retrieval, and saponin

in 0.05% PBS was used as a detergent. Slices were incubated with LipidTOX (Thermo Fisher Scientific, 10242283; 1:1000 dilution) for 30 min at RT and counterstained with Hoechst (Invitrogen; 1:1000 dilution) for 30 min at RT.

Lipid peroxidation measured using HPLC

Tissues were lysed with a KPi-EDTA buffer [50 mM KPi and 1 mM EDTA (pH 7.4)], and lipid peroxidation was determined as MDA levels, which were detected using high-performance liquid chromatography (HPLC) as an MDA–thiobarbituric acid (TBA) adduct following a method described previously (*71*). This method is based on the hydrolysis of lipoperoxides and the subsequent formation of an adduct between TBA and MDA (TBA-MDA2). This adduct was detected using HPLC in the reverse phase and quantified at 532 nm. The chromatographic technique was performed under isocratic conditions, the mobile phase being a mixture of monopotassium phosphate at 50 mM (pH 6.8) and acetonitrile (70:30). The level of MDA in each sample was divided by the concentration of protein determined by the Lowry method.

Immunoblotting for protein oxidation

To detect total protein carbonylation by immunoblot, we used the OxyBlot Protein Oxidation Detection kit (Merck) following the manufacturer's instructions. In brief, tissues were lysed in tris/SDS/glycerol buffer, protein concentration was determined by the Lowry method, and 20 μg of proteins were separated on SDS polyacrylamide gels and transferred onto nitrocellulose membranes. The membranes were blocked with 3% BSA in TBS-t for 60 min at RT and incubated overnight at 4°C with primary antibody from the kit. Following three washes (10 min) with TBS-t, membranes were incubated with secondary antibody for 60 min at RT. Following three washes with TBS-t, membranes were developed with Luminol (Sigma-Aldrich) in the ImageQuant LAS4000 system. Images were processed in ImageJ. Ponceau staining of the membranes was used as the loading control.

Telomere length and telomere damage assays

Telomere length and the number of TIF were calculated using the immunofluorescence-FISH (IF-FISH) technique. Briefly, frozen slides of the kidney and muscle were permeabilized with 0.5% Triton X-100 and washed in PBS. After 1 hour of blocking with 5% BSA-PBS, slides were incubated with 53BP1 antibody (Novus Biologicals, NB100-304) overnight at 4°C. After several washes in PBS–0.1% Tween 20, slides were incubated in donkey anti-rabbit Alexa Fluor 488 antibody (Invitrogen, A21206) for an hour and washed again in PBS. Tissues were then fixed in 4% formaldehyde for 20 min, washed several times in PBS, and dehydrated in a 70%-90%-100% ethanol series (5 min each). Slides were left to air dry, and 30 μl of telomere probe mix [10 mM tris-Cl (pH 7), 25 mM $MgCl_2$, 9 mM citric acid, 82 mM Na_2HPO_4, 50% deionized formamide (Ambion AM9342), 0.25% blocking reagent (Roche 11096176001), and telomeric PNA-Cy3 probe (0.5 μg/ml; Panagene)] was added to each slide. A coverslip was added, and slides were incubated for 3 min at 85°C and a further 2 hours at RT in a wet chamber in the dark. Slides were washed two times for 15 min in 10 mM tris-Cl (pH 7), were vigorously shaken with 0.1% BSA in 50% formamide, then washed three times for 5 min in TBS 0.08% Tween 20, and were rinsed in PBS. Slides were mounted in VECTASHIELD with 4′,6-diamidino-2-phenylindole (Vector H-1200-10). Confocal images were acquired as stacks using a Leica SP5-MP confocal microscope, and maximum projections were done with the LAS-AF software. Telomere signal intensity was quantified using Definiens software, and sites of colocalization of telomeric PNA-Cy3 probe and 53BP1 fluorescent signals were counted per cell. Image analysis was performed blindly.

SASP factor quantification

We used two commercial enzyme-linked immunosorbent assay kits for the quantitative assessment of IL-6 (Abcam, ab100713) and IL-1β (Abcam, ab197742) following the manufacturer's instructions. In brief, tissues were lysed with a specific buffer contained in each kit, protein concentration was determined by the Lowry method, and samples were diluted at 1:5 for muscle and 1:4 for the kidney. Supernatants from the C2C12 cells treated with palbociclib were obtained after treatment with sEVs or PBS and were assessed directly. Absorbance at 450 nm was measured in Molecular Devices SPECTRAmax Plus 384. All samples were assayed in duplicate.

In vitro model of senescence in muscle progenitor cells

For the in vitro experiments, we used the cell line C2C12 [American Type Culture Collection (ATCC) CRL-1772], a mouse myoblast established line. The culture medium used for the expansion and maintenance of the cells was high-glucose DMEM with 10% FBS and 1% P/S. Cells were maintained at 37°C, with 5% CO_2. Cells were seeded at a density of 10,000 cells/cm^2, and 24 hours after seeding, they were treated with 5 μM palbociclib for 96 hours. Seventy-two hours after seeding, myoblasts were treated for 48 hours in an EV-depleted culture medium with ADSC-sEVs, 3T3-sEVs, or C2C12-sEVs (5 μg/ml) in PBS or PBS alone. After that, cells were collected for further analysis by flow cytometry and immunofluorescence.

Flow cytometry analysis of C2C12 cells

To determine cellular levels of SABG, we used the FluoReporter lacZ Flow Cytometry Kit (Invitrogen) following the manufacturer's instructions. In brief, we harvested cells from the cell culture plate and diluted them to 1000 cells/μl in a staining medium and introduced a 1:1 volume of fluorescein di-β-D-galactopyranoside (FDG) 2 mM working solution; cells were stained for exactly 1 min at 37°C. FDG loading was interrupted by adding 1.8 ml of ice-cold staining medium containing 1.5 μM propidium iodide. Fluorescence values were read by FACSVerse flow cytometry (BD Biosciences, San Diego, CA, USA) until 10,000 events were recorded.

Apoptosis was assessed using an Annexin V-FITC Apoptosis detection kit (Immunostep, Salamanca, Spain), following the manufacturer's instructions. ADSCs were harvested and diluted to 1000 cells/μl in annexin-binding buffer. Then, 100 μl of aliquots of resuspended cells were placed into an appropriate flow cytometer tube and stained with 5 μl of annexin V–FITC and 5 μl of propidium iodide for exactly 15 min at 37°C in darkness. After incubation, 400 μl of 1× annexin-binding buffer was added. The values were read by FACSVerse flow cytometry (BD Biosciences, San Diego, CA, USA) until 10,000 events were recorded.

Immunofluorescence analysis of C2C12 cells

Cells were fixed with 2% PFA for 10 min at RT and permeabilized with 1% Triton X-100 in PBS for 10 min. Cells were blocked with 10% normal goat serum (Invitrogen) in PBS-t and incubated with anti-Ki67 antibody (anti-Ki67; Thermo Fisher Scientific, PA5-19462; 1:1000 dilution) overnight at 4°C. After incubation with primary

antibody, sections were washed three times with PBS-t and incubated with secondary antibody [Alexa Fluor 488 anti-rabbit (Abcam, ab150079; 1:2000 dilution)] for 2 hours at RT, washes were repeated, and cells were counterstained with Hoechst (Invitrogen; 1:1000 dilution) for 30 min at RT. Images were acquired with a LEICA DMI 3000-B fluorescence microscope. Images were processed in ImageJ, all levels were adjusted equally, and the ratios were not altered. A minimum of 200 nuclei were analyzed per sample.

sEV isolation from other cell types

We used two additional cell lines to test the effect of in vitro sEV treatment in senescence. C2C12 and 3T3 (ATCC CRL-1658) cells were expanded until they reached 80% confluency in high-glucose DMEM with 10% FBS; at that moment, medium was changed to high-glucose DMEM with 2% exosome-depleted FBS (Gibco, A2720803) and 1% P/S. After 48 hours, conditioned medium was collected, and sEVs were isolated by differential ultracentrifugation using the same method described above for the ADSCs.

Epigenetic age estimation using epigenetic clocks

DNA from different tissues was obtained using the Qiagen DNeasy Blood and Tissue Kit, following the manufacturer's instructions. Raw files were processed using the R package SeSaMe version 1.3.0 (*72*). The beta values were obtained using the default sesame procedure with nondetection.mask and quality.mask set to FALSE. Differentially methylated cytosines were detected using robust linear regression implemented in R package limma separately for each tissue. The treatment effect was estimated for each CpG by adjusting for potential confounding from age, sex, and sentrix array row. Obtained *P* values were corrected for multiple testing using the FDR procedure, and those with $q < 0.05$ were deemed significant. Pathway enrichment analysis was performed by annotating the loci to the nearest gene and ranking them by signed log *P* value. The ranked list was passed to g:profiler for enrichment analysis using R package gprofiler2 (*46*).

Multiple mouse age predictors (epigenetic clocks) were used to estimate the age of the animals. The mouse clocks were trained/developed in a separate dataset (*73*). The age predictors were grouped into general and intervention clocks. In the general group, the clocks were trained on the following mouse tissues across a wide spectrum of animals: blood, liver, brain, cerebellum, cortex, fibroblast, heart, kidney, muscle, skin, striatum, tail, and a pan tissue clock spanning all different tissues. In the intervention group, the clocks were trained across the same tissues and animals, but the loci used for training were those known to change methylation levels upon known age-affecting interventions. The effect of ADSC-sEV treatment was estimated by fitting a mixed-effects model for each tissue and group of clocks where animal age, sex, and treatment were fixed variables and clock name was a random variable. Age predicted by the clock was the response variable for the model. The statistical significance of each fixed variable was evaluated using Satterthwaite's method implemented in R package lmerTest. Array normalization, array manifest file, array annotation files, and epigenetic clock coefficients were obtained from S.H.'s laboratory. The methylation data were generated using the mammalian array platform (HorvathMammalMethylChip40) (*74*).

Plasma metabolites by proton NMR spectroscopy

For each sample, a mixture of 20 μl of blood plasma and 2 μl of phosphate buffer with trimethylsilyl propanoic acid and deuterated water was transferred into a 1-mm high-quality nuclear magnetic resonance (NMR) individual tube. Proton NMR spectra for all samples were recorded in a Bruker Avance DRX 600 spectrometer, equipped with a triple resonance 1H/13C/31P probe. The nominal temperature of the sample was kept at 310 K. A single-pulse presaturation experiment was acquired in all samples. The number of transients was 256 collected into 65 *k* data points for all experiments. Spectral chemical shift referencing on the alanine CH3 doublet signal at 1.475 parts per million (ppm) was performed in all spectra. Spectra were processed using MestReNova 8.1 (Mestrelab Research S.L., Spain) and transferred to MATLAB (MathWorks, 2012) using in-house scripts for data analysis. The chemical shift region including resonances 0.50 to 4.70 ppm (the aliphatic region) and 5.20 to 10.00 ppm (the aromatic region) was investigated. Metabolite spin systems and resonances were identified by literature data and the Chenomx resonances database (Chenomx NMR 7.6). Spectra were normalized to the total aliphatic spectral area, lipid excluded, to eliminate differences in metabolite total concentration. NMR peaks were integrated and quantified using semiautomated in-house MATLAB peak-fitting routines. Final metabolite levels were calculated in arbitrary units as peak area normalized to the total spectral area. Chemometric analysis was performed with PLS ToolBox 8.0 (Eigenvector Inc.) in MATLAB. To maximize the separation between samples and to identify discriminant patterns, PLS-DA was applied. The permutation test was performed to check the overfitting of the PLS-DA models. The multivariate chemometric models were cross-validated with 10-fold Venetian blind cross-validation. In each run, 10% of the data were left out of the training and used to test the model. Spectral regions with high VIP coefficients obtained during PLS-DA are more important in providing class separation during analysis, while those with very small VIP coefficients provide little contribution to classification. An MSEA over metabolites with VIP scores higher than 0.5 and *P* values below 0.05 was performed with MetaboAnalyst and the SMPDB. MSEA is conceptually like gene set enrichment analysis and uses a collection of predefined metabolites sets to rank the lists of metabolites obtained from metabolomics studies. By using this prior knowledge about metabolite sets, we could identify significant and coordinated changes in metabolic networks and obtain biological insight.

Total RNA extraction from sEVs and small noncoding RNA expression profiling

sEVs obtained from different sources were stored in PBS at −80°C; for the isolation of RNA, we used the Total Exosome RNA Protein Isolation Kit (Thermo Fisher Scientific), following the manufacturer's instructions.

Small noncoding RNA expression profiling was performed using a GeneChip miRNA 4.0 Array (Affymetrix, Santa Clara, CA, USA). Microarray experiments were conducted according to the manufacturer's protocol. Briefly, 130 ng of total RNA was labeled with a FlashTag Biotin HSR RNA labeling kit from Genisphere. The labeling reaction was hybridized onto the miRNA array in an Affymetrix hybridization oven 645 at 48°C for 18 hours. The arrays were stained using a Fluidics Station 450 with the fluidics script FS450_0002 (Affymetrix) and then scanned on a GeneChip Scanner 3000 7G (Affymetrix, Santa Clara, CA, USA), using the GeneChip Command Console Software supplied by Affymetrix to perform gene expression analysis. MiRNA probe outliers were defined and further analyzed as per the manufacturer's instructions (Affymetrix), and quality control, as well as data summarization and normalization, was carried out using the web-based miRNA QC Tool (www.affymetrix.com).

miRNA expression levels were analyzed with Transcriptome Analysis Suite (Thermo Fisher Scientific). Data (.CEL files) were analyzed and statistically filtered using Transcriptome Analysis Suite (Thermo Fisher Scientific), and input files were normalized with the robust multi-array analysis (RMA) for miRNAs. A one-way analysis of variance (ANOVA) was performed with the Transcriptome Analysis Suite (Thermo Fisher Scientific) on all samples. Statistically significant small noncoding RNAs between the different groups and treatments studied were identified using an analysis of the variance model with a P value of 0.01 or less. The imported data were analyzed by PCA to determine the significant sources of variability in the data.

miRNA pathway and biological process analysis

From the up-regulated miRNAs comparing sEVs from young ADSCs to old mice's plasmatic sEVs, the six miRNAs conserved across species were analyzed using mirDIP to determine miRNA target genes with very high confidence (top 1% in confidence). A total of 5379 unique genes were further analyzed by PANTHER to identify enriched biological pathways and biological processes with an overrepresentation test; in PANTHER, Fisher's exact test was used with FDR correction. P value < 0.01 was considered statistically significant. For the biological process analysis, we considered only processes with twofold enrichment or more.

In vitro miRNA mimics treatment

To test the effect of our selected miRNAs in vitro, we treated senescent C2C12 cells using the same culture method as the one described above for the in vitro model of senescence. Cells were seeded at a density of 10,000 cells/cm^2, and 24 hours after seeding, they were treated with 5 μM palbociclib for 96 hours. Seventy-two hours after seeding, myoblasts were transfected for 48 hours in an EV-depleted culture medium with 1 μM miRNA mimic or small interfering RNA control (Qiagen, 1027280) using HIPerFect Transfection Reagent (Qiagen, 301704). After that, cells were collected for further analysis by flow cytometry. Mimics used: Syn-mmu-miR-125b-5p miScript miRNA Mimic (Qiagen, MSY0000136/S0), Syn-mmu-miR-let7c-5p miScript miRNA Mimic (Qiagen, MSY0000523/S0), Syn-mmu-miR-214-3p miScript miRNA Mimic (Qiagen, MSY0000661/S0), Syn-mmu-miR-145a-5p miScript miRNA Mimic (Qiagen, MSY0000157/S0), Syn-mmu-miR-135a-1-3p miScript miRNA Mimic (Qiagen, MSY0004531/S0), and Syn-mmu-miR-143-3p miScript miRNA Mimic (Qiagen, MSY0000247/S0).

Statistical analysis

Ratios comparing physical test and plasma values after treatment compared to baseline were determined and plotted as % over baseline. The baseline was defined as 0%. All groups were tested for the presence of outliers with the ROUT method (Q = 2%), and just one data point was excluded from the analysis; these data came from a mouse in the PBS group that showed about 80% decline in the Treadmill test at day 30. Saphiro-Wilk test was conducted in each comparison to test the normality of each group. Unpaired Student's t test or Mann-Whitney test was used to calculate the P value for pairwise comparisons. For the in vitro experiments with multiple comparisons, ANOVA was used with Tukey's multiple comparisons as a post hoc test; in case of nonparametric data, Kruskal-Wallis test was used with Dunn's multiple comparisons as a post hoc test. Each data point presented throughout the manuscript refers to biological replicates; technical replicates are described in the Materials and Methods. GraphPad Prism 9.0 software was used for the analysis and graphical design.

SUPPLEMENTARY MATERIALS

Supplementary material for this article is available at https://science.org/doi/10.1126/sciadv.abq2226

View/request a protocol for this paper from *Bio-protocol*.

REFERENCES AND NOTES

1. L. P. Fried, C. M. Tangen, J. Walston, A. B. Newman, C. Hirsch, J. Gottdiener, T. Seeman, R. Tracy, W. J. Kop, G. Burke, M. A. McBurnie; Cardiovascular Health Study Collaborative Research Group, Frailty in older adults: Evidence for a phenotype. *J. Gerontol. A Biol. Sci. Med. Sci.* **56**, M146–M157 (2001).
2. C. Lopez-Otin, M. A. Blasco, L. Partridge, M. Serrano, G. Kroemer, The hallmarks of aging. *Cell* **153**, 1194–1217 (2013).
3. F. Lauretani, C. R. Russo, S. Bandinelli, B. Bartali, C. Cavazzini, A. D. Iorio, A. M. Corsi, T. Rantanen, J. M. Guralnik, L. Ferrucci, Age-associated changes in skeletal muscles and their effect on mobility: An operational diagnosis of sarcopenia. *J. Appl. Physiol. (1985)* **95**, 1851–1860 (2003).
4. A. Denic, R. J. Glassock, A. D. Rule, Structural and functional changes with the aging kidney. *Adv. Chronic Kidney Dis.* **23**, 19–28 (2016).
5. S. J. Russell, C. R. Kahn, Endocrine regulation of ageing. *Nat. Rev. Mol. Cell Biol.* **8**, 681–691 (2007).
6. C. Franceschi, M. Bonafè, S. Valensin, F. Olivieri, M. de Luca, E. Ottaviani, G. de Benedictis, Inflamm-aging. An evolutionary perspective on immunosenescence. *Ann. N. Y. Acad. Sci.* **908**, 244–254 (2000).
7. C. Franceschi, J. Campisi, Chronic inflammation (inflammaging) and its potential contribution to age-associated diseases. *J. Gerontol. A Biol. Sci. Med. Sci.* **69** (Suppl. 1), S4–S9 (2014).
8. G. Zhang, J. Li, S. Purkayastha, Y. Tang, H. Zhang, Y. Yin, B. Li, G. Liu, D. Cai, Hypothalamic programming of systemic ageing involving IKK-β, NF-κB and GnRH. *Nature* **497**, 211–216 (2013).
9. C. M. Mccay, F. Pope, W. Lunsford, G. Sperling, P. Sambhavaphol, Parabiosis between old and young rats. *Gerontologia* **1**, 7–17 (1957).
10. I. M. Conboy, M. J. Conboy, A. J. Wagers, E. R. Girma, I. L. Weissman, T. A. Rando, Rejuvenation of aged progenitor cells by exposure to a young systemic environment. *Nature* **433**, 760–764 (2005).
11. F. S. Loffredo, M. L. Steinhauser, S. M. Jay, J. Gannon, J. R. Pancoast, P. Yalamanchi, M. Sinha, C. Dall'Osso, D. Khong, J. L. Shadrach, C. M. Miller, B. S. Singer, A. Stewart, N. Psychogios, R. E. Gerszten, A. J. Hartigan, M. J. Kim, T. Serwold, A. J. Wagers, R. T. Lee, Growth differentiation factor 11 is a circulating factor that reverses age-related cardiac hypertrophy. *Cell* **153**, 828–839 (2013).
12. J. Durieux, S. Wolff, A. Dillin, The cell-non-autonomous nature of electron transport chain-mediated longevity. *Cell* **144**, 79–91 (2011).
13. M. Lavasani, A. R. Robinson, A. Lu, M. Song, J. M. Feduska, B. Ahani, J. S. Tilstra, C. H. Feldman, P. D. Robbins, L. J. Niedernhofer, J. Huard, Muscle-derived stem/progenitor cell dysfunction limits healthspan and lifespan in a murine progeria model. *Nat. Commun.* **3**, 608 (2012).
14. A. Tomás-Loba, I. Flores, P. J. Fernández-Marcos, M. L. Cayuela, A. Maraver, A. Tejera, C. Borrás, A. Matheu, P. Klatt, J. M. Flores, J. Viña, M. Serrano, M. A. Blasco, Telomerase reverse transcriptase delays aging in cancer-resistant mice. *Cell* **135**, 609–622 (2008).
15. A. K. Ludwig, B. Giebel, Exosomes: Small vesicles participating in intercellular communication. *Int. J. Biochem. Cell Biol.* **44**, 11–15 (2012).
16. G. Maguire, Stem cell therapy without the cells. *Commun. Integr. Biol.* **6**, e26631 (2013).
17. L. Chen, E. E. Tredget, P. Y. Wu, Y. Wu, Paracrine factors of mesenchymal stem cells recruit macrophages and endothelial lineage cells and enhance wound healing. *PLOS ONE* **3**, e1886 (2008).
18. R. C. Lai, F. Arslan, M. M. Lee, N. S. K. Sze, A. Choo, T. S. Chen, M. Salto-Tellez, L. Timmers, C. N. Lee, R. M. el Oakley, G. Pasterkamp, D. P. V. de Kleijn, S. K. Lim, Exosome secreted by MSC reduces myocardial ischemia/reperfusion injury. *Stem Cell Res.* **4**, 214–222 (2010).
19. C. Y. Tan, R. C. Lai, W. Wong, Y. Y. Dan, S. K. Lim, H. K. Ho, Mesenchymal stem cell-derived exosomes promote hepatic regeneration in drug-induced liver injury models. *Stem Cell Res. Ther.* **5**, 76 (2014).
20. B. Yu, X. Zhang, X. Li, Exosomes derived from mesenchymal stem cells. *Int. J. Mol. Sci.* **15**, 4142–4157 (2014).
21. L. Barile, G. Vassalli, Exosomes: Therapy delivery tools and biomarkers of diseases. *Pharmacol. Ther.* **174**, 63–78 (2017).
22. R. C. Lai, R. W. Yeo, K. H. Tan, S. K. Lim, Exosomes for drug delivery - A novel application for the mesenchymal stem cell. *Biotechnol. Adv.* **31**, 543–551 (2013).

23. R. W. Y. Yeo, R. C. Lai, B. Zhang, S. S. Tan, Y. Yin, B. J. Teh, S. K. Lim, Mesenchymal stem cell: An efficient mass producer of exosomes for drug delivery. *Adv. Drug Deliv. Rev.* **65**, 336–341 (2013).
24. C. Mas-Bargues, J. Sanz-Ros, A. Román-Domínguez, M. Inglés, L. Gimeno-Mallench, M. el Alami, J. Viña-Almunia, J. Gambini, J. Viña, C. Borrás, Relevance of oxygen concentration in stem cell culture for regenerative medicine. *Int. J. Mol. Sci.* **20**, 1195 (2019).
25. C. Mas-Bargues, J. Sanz-Ros, A. Román-Domínguez, L. Gimeno-Mallench, M. Inglés, J. Viña, C. Borrás, Extracellular vesicles from healthy cells improves cell function and stemness in premature senescent stem cells by miR-302b and HIF-1α activation. *Biomolecules* **10**, 957 (2020).
26. C. Mas-Bargues, C. Borrás, Importance of stem cell culture conditions for their derived extracellular vesicles therapeutic effect. *Free Radic. Biol. Med.* **168**, 16–24 (2021).
27. Y. Zhang, M. S. Kim, B. Jia, J. Yan, J. P. Zuniga-Hertz, C. Han, D. Cai, Hypothalamic stem cells control ageing speed partly through exosomal miRNAs. *Nature* **548**, 52–57 (2017).
28. M. Borghesan, J. Fafián-Labora, O. Eleftheriadou, P. Carpintero-Fernández, M. Paez-Ribes, G. Vizcay-Barrena, A. Swisa, D. Kolodkin-Gal, P. Ximénez-Embún, R. Lowe, B. Martín-Martín, H. Peinado, J. Muñoz, R. A. Fleck, Y. Dor, I. Ben-Porath, A. Vossenkamper, D. Muñoz-Espin, A. O'Loghlen, Small extracellular vesicles are key regulators of non-cell autonomous intercellular communication in senescence via the interferon protein IFITM3. *Cell Rep.* **27**, 3956–3971.e6 (2019).
29. J. A. Fafián-Labora, J. A. Rodríguez-Navarro, A. O'Loghlen, Small extracellular vesicles have GST activity and ameliorate senescence-related tissue damage. *Cell Metab.* **32**, 71–86.e5 (2020).
30. B. R. Lee, J. H. Kim, E. S. Choi, J. H. Cho, E. Kim, Effect of young exosomes injected in aged mice. *Int. J. Nanomedicine* **13**, 5335–5345 (2018).
31. M. Yoshida, A. Satoh, J. B. Lin, K. F. Mills, Y. Sasaki, N. Rensing, M. Wong, R. S. Apte, S.-I. Imai, Extracellular vesicle-contained eNAMPT delays aging and extends lifespan in mice. *Cell Metab.* **30**, 329–342.e5 (2019).
32. C. Théry, K. W. Witwer, E. Aikawa, M. J. Alcaraz, J. D. Anderson, R. Andriantsitohaina, A. Antoniou, T. Arab, F. Archer, G. K. Atkin-Smith, D. C. Ayre, J. M. Bach, D. Bachurski, H. Baharvand, L. Balaj, S. Baldacchino, N. N. Bauer, A. A. Baxter, M. Bebawy, C. Beckham, A. Bedina Zavec, A. Benmoussa, A. C. Berardi, P. Bergese, E. Bielska, C. Blenkiron, S. Bobis-Wozowicz, E. Boilard, W. Boireau, A. Bongiovanni, F. E. Borràs, S. Bosch, C. M. Boulanger, X. Breakefield, A. M. Breglio, M. Á. Brennan, D. R. Brigstock, A. Brisson, M. L. D. Broekman, J. F. Bromberg, P. Bryl-Górecka, S. Buch, A. H. Buck, D. Burger, S. Busatto, D. Buschmann, B. Bussolati, E. I. Buzás, J. B. Byrd, G. Camussi, D. R. F. Carter, S. Caruso, L. W. Chamley, Y. T. Chang, C. Chen, S. Chen, L. Cheng, A. R. Chin, A. Clayton, S. P. Clerici, A. Cocks, E. Cocucci, R. J. Coffey, A. Cordeiro-da-Silva, Y. Couch, F. A. W. Coumans, B. Coyle, R. Crescitelli, M. F. Criado, C. D'Souza-Schorey, S. das, A. D. Chaudhuri, P. de Candia, E. F. de Santana Jr., O. de Wever, H. A. del Portillo, T. Demaret, S. Deville, A. Devitt, B. Dhondt, D. di Vizio, L. C. Dieterich, V. Dolo, A. P. D. Rubio, M. Dominici, M. R. Dourado, T. A. P. Driedonks, F. V. Duarte, H. M. Duncan, R. M. Eichenberger, K. Ekström, S. el Andaloussi, C. Elie-Caille, U. Erdbrügger, J. M. Falcón-Pérez, F. Fatima, J. E. Fish, M. Flores-Bellver, A. Försönits, A. Frelet-Barrand, F. Fricke, G. Fuhrmann, S. Gabrielsson, A. Gámez-Valero, C. Gardiner, K. Gärtner, R. Gaudin, Y. S. Gho, B. Giebel, C. Gilbert, M. Gimona, I. Giusti, D. C. I. Goberdhan, A. Görgens, S. M. Gorski, D. W. Greening, J. C. Gross, A. Gualerzi, G. N. Gupta, D. Gustafson, A. Handberg, R. A. Haraszti, P. Harrison, H. Hegyesi, A. Hendrix, A. F. Hill, F. H. Hochberg, K. F. Hoffmann, B. Holder, H. Holthofer, B. Hosseinkhani, G. Hu, Y. Huang, V. Huber, S. Hunt, A. G. E. Ibrahim, T. Ikezu, J. M. Inal, M. Isin, A. Ivanova, H. K. Jackson, S. Jacobsen, S. M. Jay, M. Jayachandran, G. Jenster, L. Jiang, S. M. Johnson, J. C. Jones, A. Jong, T. Jovanovic-Talisman, S. Jung, R. Kalluri, S. I. Kano, S. Kaur, Y. Kawamura, E. T. Keller, D. Khamari, E. Khomyakova, A. Khvorova, P. Kierulf, K. P. Kim, T. Kislinger, M. Klingeborn, D. J. Klinke II, M. Kornek, M. M. Kosanović, Á. F. Kovács, E. M. Krämer-Albers, S. Krasemann, M. Krause, I. V. Kurochkin, G. D. Kusuma, S. Kuypers, S. Laitinen, S. M. Langevin, L. R. Languino, J. Lannigan, C. Lässer, L. C. Laurent, G. Lavieu, E. Lázaro-Ibáñez, S. le Lay, M. S. Lee, Y. X. F. Lee, D. S. Lemos, M. Lenassi, A. Leszczynska, I. T. S. Li, K. Liao, S. F. Libregts, E. Ligeti, R. Lim, S. K. Lim, A. Linē, K. Linnemannstöns, A. Llorente, C. A. Lombard, M. J. Lorenowicz, Á. M. Lörincz, J. Lötvall, J. Lovett, M. C. Lowry, X. Loyer, Q. Lu, B. Lukomska, T. R. Lunavat, S. L. N. Maas, H. Malhi, A. Marcilla, J. Mariani, J. Mariscal, E. S. Martens-Uzunova, L. Martin-Jaular, M. C. Martinez, V. R. Martins, M. Mathieu, S. Mathivanan, M. Maugeri, L. K. McGinnis, M. J. McVey, D. G. Meckes Jr., K. L. Meehan, I. Mertens, V. R. Minciacchi, A. Möller, M. M. Jørgensen, A. Morales-Kastresana, J. Morhayim, F. Mullier, M. Muraca, L. Musante, V. Mussack, D. C. Muth, K. H. Myburgh, T. Najrana, M. Nawaz, I. Nazarenko, P. Nejsum, C. Neri, T. Neri, R. Nieuwland, L. Nimrichter, J. P. Nolan, E. N. M. Nolte-'t Hoen, N. N. Hooten, L. O'Driscoll, T. O'Grady, A. O'Loghlen, T. Ochiya, M. Olivier, A. Ortiz, L. A. Ortiz, X. Osteikoetxea, O. Østergaard, M. Ostrowski, J. Park, D. M. Pegtel, H. Peinado, F. Perut, M. W. Pfaffl, D. G. Phinney, B. C. H. Pieters, R. C. Pink, D. S. Pisetsky, E. P. von Strandmann, I. Polakovicova, I. K. H. Poon, B. H. Powell, I. Prada, L. Pulliam, P. Quesenberry, A. Radeghieri, R. L. Raffai, S. Raimondo, J. Rak, M. I. Ramirez, G. Raposo, M. S. Rayyan, N. Regev-Rudzki, F. L. Ricklefs, P. D. Robbins, D. D. Roberts, S. C. Rodrigues, E. Rohde, S. Rome, K. M. A. Rouschop, A. Rughetti, A. E. Russell, P. Saá, S. Sahoo, E. Salas-Huenuleo, C. Sánchez, J. A. Saugstad, M. J. Saul, R. M. Schiffelers, R. Schneider, T. H. Schøyen, A. Scott, E. Shahaj, S. Sharma, O. Shatnyeva, F. Shekari, G. V. Shelke, A. K. Shetty, K. Shiba, P. R. M. Siljander, A. M. Silva, A. Skowronek, O. L. Snyder II, R. P. Soares, B. W. Sódar, C. Soekmadji, J. Sotillo, P. D. Stahl, W. Stoorvogel, S. L. Stott, E. F. Strasser, S. Swift, H. Tahara, M. Tewari, K. Timms, S. Tiwari, R. Tixeira, M. Tkach, W. S. Toh, R. Tomasini, A. C. Torrecilhas, J. P. Tosar, V. Toxavidis, L. Urbanelli, P. Vader, B. W. M. van Balkom, S. G. van der Grein, J. van Deun, M. J. C. van Herwijnen, K. van Keuren-Jensen, G. van Niel, M. E. van Royen, A. J. van Wijnen, M. H. Vasconcelos, I. J. Vechetti Jr., T. D. Veit, L. J. Vella, É. Velot, F. J. Verweij, B. Vestad, J. L. Viñas, T. Visnovitz, K. V. Vukman, J. Wahlgren, D. C. Watson, M. H. M. Wauben, A. Weaver, J. P. Webber, V. Weber, A. M. Wehman, D. J. Weiss, J. A. Welsh, S. Wendt, A. M. Wheelock, Z. Wiener, L. Witte, J. Wolfram, A. Xagorari, P. Xander, J. Xu, X. Yan, M. Yáñez-Mó, H. Yin, Y. Yuana, V. Zappulli, J. Zarubova, V. Žėkas, J. Y. Zhang, Z. Zhao, L. Zheng, A. R. Zheutlin, A. M. Zickler, P. Zimmermann, A. M. Zivkovic, D. Zocco, E. K. Zuba-Surma, Minimal information for studies of extracellular vesicles 2018 (MISEV2018): A position statement of the International Society for Extracellular Vesicles and update of the MISEV2014 guidelines. *J. Extracell. Vesicles* **7**, 1535750 (2018).
33. M. Zöller, Tetraspanins: Push and pull in suppressing and promoting metastasis. *Nat. Rev. Cancer* **9**, 40–55 (2009).
34. M. C. Gomez-Cabrera, R. Garcia-Valles, L. Rodriguez-Mañas, F. J. Garcia-Garcia, G. Olaso-Gonzalez, A. Salvador-Pascual, F. J. Tarazona-Santabalbina, J. Viña, A new frailty score for experimental animals based on the clinical phenotype: Inactivity as a model of frailty. *J. Gerontol. A Biol. Sci. Med. Sci.* **72**, 885–891 (2017).
35. A. Matheu, A. Maraver, P. Klatt, I. Flores, I. Garcia-Cao, C. Borras, J. M. Flores, J. Viña, M. A. Blasco, M. Serrano, Delayed ageing through damage protection by the Arf/p53 pathway. *Nature* **448**, 375–379 (2007).
36. I. M. Conboy, T. A. Rando, Aging, stem cells and tissue regeneration: Lessons from muscle. *Cell Cycle* **4**, 407–410 (2005).
37. S. S. Khan, B. D. Singer, D. E. Vaughan, Molecular and physiological manifestations and measurement of aging in humans. *Aging Cell* **16**, 624–633 (2017).
38. W. R. Hazzard, J. P. Blass, W. H. Ettinger Jr., J. B. Halter, J. Ouslander, in *Frailty and Failure to Thrive*, L. P. Fried, J. Walston, Eds. (McGraw Hill, 4 ed. 1998), pp. 1387–1402.
39. K. Berger, J. M. Bangen, L. Hammerich, C. Liedtke, J. Floege, B. Smeets, M. J. Moeller, Origin of regenerating tubular cells after acute kidney injury. *Proc. Natl. Acad. Sci. U.S.A.* **111**, 1533–1538 (2014).
40. A. J. Cruz-Jentoft, F. Landi, S. M. Schneider, C. Zúñiga, H. Arai, Y. Boirie, L.-K. Chen, R. A. Fielding, F. C. Martin, J.-P. Michel, C. Sieber, J. R. Stout, S. A. Studenski, B. Vellas, J. Woo, M. Zamboni, T. Cederholm, Prevalence of and interventions for sarcopenia in ageing adults: A systematic review. Report of the International Sarcopenia Initiative (EWGSOP and IWGS). *Age Ageing* **43**, 748–759 (2014).
41. L. Larsson, H. Degens, M. Li, L. Salviati, Y. I. Lee, W. Thompson, J. L. Kirkland, M. Sandri, Sarcopenia: Aging-related loss of muscle mass and function. *Physiol. Rev.* **99**, 427–511 (2019).
42. M. A. Blasco, Telomere length, stem cells and aging. *Nat. Chem. Biol.* **3**, 640–649 (2007).
43. J. P. Coppé, P. Y. Desprez, A. Krtolica, J. Campisi, The senescence-associated secretory phenotype: The dark side of tumor suppression. *Annu. Rev. Pathol.* **5**, 99–118 (2010).
44. J. M. van Deursen, The role of senescent cells in ageing. *Nature* **509**, 439–446 (2014).
45. A. Freund, R. M. Laberge, M. Demaria, J. Campisi, Lamin B1 loss is a senescence-associated biomarker. *Mol. Biol. Cell* **23**, 2066–2075 (2012).
46. U. Raudvere, L. Kolberg, I. Kuzmin, T. Arak, P. Adler, H. Peterson, J. Vilo, g:Profiler: A web server for functional enrichment analysis and conversions of gene lists (2019 update). *Nucleic Acids Res.* **47**, W191–W198 (2019).
47. Z. Y. Zhang, D. Monleon, P. Verhamme, J. A. Staessen, Branched-chain amino acids as critical switches in health and disease. *Hypertension* **72**, 1012–1022 (2018).
48. H. Mangge, I. Stelzer, E. Z. Reininghaus, D. Weghuber, T. T. Postolache, D. Fuchs, Disturbed tryptophan metabolism in cardiovascular disease. *Curr. Med. Chem.* **21**, 1931–1937 (2014).
49. F. Moens, M. Verce, L. De Vuyst, Lactate- and acetate-based cross-feeding interactions between selected strains of lactobacilli, bifidobacteria and colon bacteria in the presence of inulin-type fructans. *Int. J. Food Microbiol.* **241**, 225–236 (2017).
50. X. Liu, J. Gao, J. Chen, Z. Wang, Q. Shi, H. Man, S. Guo, Y. Wang, Z. Li, W. Wang, Identification of metabolic biomarkers in patients with type 2 diabetic coronary heart diseases based on metabolomic approach. *Sci. Rep.* **6**, 30785 (2016).
51. A. Barbul, Proline precursors to sustain Mammalian collagen synthesis. *J. Nutr.* **138**, 2021S–2024S (2008).
52. T. Thomou, M. A. Mori, J. M. Dreyfuss, M. Konishi, M. Sakaguchi, C. Wolfrum, T. N. Rao, J. N. Winnay, R. Garcia-Martin, S. K. Grinspoon, P. Gorden, C. R. Kahn, Adipose-derived circulating miRNAs regulate gene expression in other tissues. *Nature* **542**, 450–455 (2017).
53. C. Borrás, E. Serna, J. Gambini, M. Inglés, J. Vina, Centenarians maintain miRNA biogenesis pathway while it is impaired in octogenarians. *Mech. Ageing Dev.* **168**, 54–57 (2017).

54. E. Serna, J. Gambini, C. Borras, K. M. Abdelaziz, A. Belenguer, P. Sanchis, J. A. Avellana, L. Rodriguez-Mañas, J. Viña, Centenarians, but not octogenarians, up-regulate the expression of microRNAs. *Sci. Rep.* **2**, 961 (2012).
55. M. A. Mori, P. Raghavan, T. Thomou, J. Boucher, S. Robida-Stubbs, Y. Macotela, S. J. Russell, J. L. Kirkland, T. K. Blackwell, C. R. Kahn, Role of microRNA processing in adipose tissue in stress defense and longevity. *Cell Metab.* **16**, 336–347 (2012).
56. E. D. Smith, M. Tsuchiya, L. A. Fox, N. Dang, D. Hu, E. O. Kerr, E. D. Johnston, B. N. Tchao, D. N. Pak, K. L. Welton, D. E. L. Promislow, J. H. Thomas, M. Kaeberlein, B. K. Kennedy, Quantitative evidence for conserved longevity pathways between divergent eukaryotic species. *Genome Res.* **18**, 564–570 (2008).
57. H. Mi, A. Muruganujan, J. T. Casagrande, P. D. Thomas, Large-scale gene function analysis with the PANTHER classification system. *Nat. Protoc.* **8**, 1551–1566 (2013).
58. P. Sousa-Victor, J. Neves, W. Cedron-Craft, P. B. Ventura, C. Y. Liao, R. R. Riley, I. Soifer, N. van Bruggen, G. A. Kolumam, S. A. Villeda, D. A. Lamba, H. Jasper, MANF regulates metabolic and immune homeostasis in ageing and protects against liver damage. *Nat. Metab.* **1**, 276–290 (2019).
59. L. Hu, J. Wang, X. Zhou, Z. Xiong, J. Zhao, R. Yu, F. Huang, H. Zhang, L. Chen, Exosomes derived from human adipose mensenchymal stem cells accelerates cutaneous wound healing via optimizing the characteristics of fibroblasts. *Sci. Rep.* **6**, 32993 (2016).
60. A. Dorronsoro, F. E. Santiago, D. Grassi, T. Zhang, R. C. Lai, S. J. McGowan, L. Angelini, M. Lavasani, L. Corbo, A. Lu, R. W. Brooks, M. Garcia-Contreras, D. B. Stolz, A. Amelio, S. V. Boregowda, M. Fallahi, A. Reich, C. Ricordi, D. G. Phinney, J. Huard, S. K. Lim, L. J. Niedernhofer, P. D. Robbins, Mesenchymal stem cell-derived extracellular vesicles reduce senescence and extend health span in mouse models of aging. *Aging Cell* **20**, e13337 (2021).
61. P. Muñoz-Cánoves, C. Scheele, B. K. Pedersen, A. L. Serrano, Interleukin-6 myokine signaling in skeletal muscle: A double-edged sword? *FEBS J.* **280**, 4131–4148 (2013).
62. S. Horvath, DNA methylation age of human tissues and cell types. *Genome Biol.* **14**, R115 (2013).
63. D. A. Petkovich, D. I. Podolskiy, A. V. Lobanov, S.-G. Lee, R. A. Miller, V. N. Gladyshev, Using DNA methylation profiling to evaluate biological age and longevity interventions. *Cell Metab.* **25**, 954–960.e6 (2017).
64. S. Maegawa, Y. Lu, T. Tahara, J. T. Lee, J. Madzo, S. Liang, J. Jelinek, R. J. Colman, J. P. J. Issa, Caloric restriction delays age-related methylation drift. *Nat. Commun.* **8**, 539 (2017).
65. T. Wang, B. Tsui, J. F. Kreisberg, N. A. Robertson, A. M. Gross, M. K. Yu, H. Carter, H. M. Brown-Borg, P. D. Adams, T. Ideker, Epigenetic aging signatures in mice livers are slowed by dwarfism, calorie restriction and rapamycin treatment. *Genome Biol.* **18**, 57 (2017).
66. B. W. M. van Balkom, O. G. de Jong, M. Smits, J. Brummelman, K. den Ouden, P. M. de Bree, M. A. J. van Eijndhoven, D. M. Pegtel, W. Stoorvogel, T. Würdinger, M. C. Verhaar, Endothelial cells require miR-214 to secrete exosomes that suppress senescence and induce angiogenesis in human and mouse endothelial cells. *Blood* **121**, 3997–4006 (2013).
67. X. Lei, N. He, L. Zhu, M. Zhou, K. Zhang, C. Wang, H. Huang, S. Chen, Y. Li, Q. Liu, Z. Han, Z. Guo, Z. Han, Z. Li, Mesenchymal stem cell-derived extracellular vesicles attenuate radiation-induced lung injury. *Antioxid. Redox Signal.* **35**, 849–862 (2020).
68. J. R. Chevillet, Q. Kang, I. K. Ruf, H. A. Briggs, L. N. Vojtech, S. M. Hughes, H. H. Cheng, J. D. Arroyo, E. K. Meredith, E. N. Gallichotte, E. L. Pogosova-Agadjanyan, C. Morrissey, D. L. Stirewalt, F. Hladik, E. Y. Yu, C. S. Higano, M. Tewari, Quantitative and stoichiometric analysis of the microRNA content of exosomes. *Proc. Natl. Acad. Sci. U.S.A.* **111**, 14888–14893 (2014).
69. M. Albanese, Y. F. A. Chen, C. Hüls, K. Gärtner, T. Tagawa, E. Mejias-Perez, O. T. Keppler, C. Göbel, R. Zeidler, M. Shein, A. K. Schütz, W. Hammerschmidt, MicroRNAs are minor constituents of extracellular vesicles that are rarely delivered to target cells. *PLOS Genet.* **17**, e1009951 (2021).
70. G. Yu, X. Wu, G. Kilroy, Y. D. C. Halvorsen, J. M. Gimble, Z. E. Floyd, Isolation of murine adipose-derived stem cells. *Methods Mol. Biol.* **702**, 29–36 (2011).
71. C. Mas-Bargues, J. Viña-Almunia, M. Inglés, J. Sanz-Ros, J. Gambini, J. S. Ibáñez-Cabellos, J. L. García-Giménez, J. Viña, C. Borrás, Role of p16INK4a and BMI-1 in oxidative stress-induced premature senescence in human dental pulp stem cells. *Redox Biol.* **12**, 690–698 (2017).
72. W. Zhou, T. J. Triche, P. W. Laird, H. Shen, SeSAMe: Reducing artifactual detection of DNA methylation by infinium BeadChips in genomic deletions. *Nucleic Acids Res.* **46**, e123 (2018).
73. K. Mozhui, A. T. Lu, C. Z. Li, A. Haghani, J. V. Sandoval-Sierra, Y. Wu, R. W. Williams, S. Horvath, Genetic loci and metabolic states associated with murine epigenetic aging. *eLife* **11**, e75244 (2022).
74. A. Arneson, A. Haghani, M. J. Thompson, M. Pellegrini, S. B. Kwon, H. Vu, E. Maciejewski, M. Yao, C. Z. Li, A. T. Lu, M. Morselli, L. Rubbi, B. Barnes, K. D. Hansen, W. Zhou, C. E. Breeze, J. Ernst, S. Horvath, A mammalian methylation array for profiling methylation levels at conserved sequences. *Nat. Commun.* **13**, 783 (2022).

Acknowledgments: We appreciate the contribution of the Flow Cytometry Service, Multigenic Analysis Unit, Animal Facility, and Metabolomic and Molecular Image Laboratory of the Central Unit in Medical Research, as well as the Microscopy section of the Central Service of Support to the Experimental Research, of the University of Valencia. We also want to thank the help provided by the Electronic Microscopy service of the Príncipe Felipe Research Centre in Valencia. We also thank M. Noyes for the help in reviewing the manuscript. **Funding:** This work was supported by the following grants: CB16/10/00435 (CIBERFES) from Instituto de Salud Carlos III, PID2019-110906RB-I00/AEI/10.13039/501100011033 and RED2018-102576-T from the Spanish Ministry of Innovation and Science, PROMETEO/2019/097 from "Consellería, de Educació de la Generalitat Valenciana," EU Funded H2020 - DIABFRAIL-LATAM (Ref: 825546), European Joint Programming Initiative "A Healthy Diet for a Healthy Life" (JPI HDHL), the ERA-NET Cofund ERA-HDHL (grant agreement no. 696295 of the EU Horizon 2020 Research and Innovation Programme), and Fundación Ramón Areces y Fundación Soria Melguizo to J.V; PID2019-108973RB-C22 to D.M; grant PID2020-113839RB-I00 funded by MCIN/AEI/10.13039/501100011033, PCIN-2017-117 of the Ministry of Economy and Competitiveness, and the EU Joint Programming Initiative "A Healthy Diet for a Healthy Life" (JPI HDHL INTIMIC-085) to C.B. Part of the equipment used in this work has been funded by Generalitat Valenciana and cofinanced with ERDF funds (OP ERDF of Comunitat Valenciana 2014-2020). **Author contributions:** Conceptualization: J.S.-R., J.V., and C.B. Methodology: J.S.-R., N.R.-G., D.M., J.G., R.T.B., A.G.-C., and A.R.-D. Investigation: J.S.-R., N.R.-G., C.M.-B., D.M., J.G., R.T.B., M.D., A.Dí., A.De., A.G.-C., A.R.-D., and M.I. Visualization: J.S.-R. and C.B. Supervision: M.A.B., S.H., J.V., and C.B. Writing—original draft: J.S.-R., D.M., J.G., and C.B. Writing—review and editing: M.A.B., S.H., J.V., and C.B. **Competing interests:** S.H. is a founder of the nonprofit Epigenetic Clock Development Foundation that distributes the mammalian methylation array platform (HorvathMammalMethylChip40) used here. The other authors declare that they have no competing interests. **Data and materials availability:** sEV isolation and characterization methodology has been updated to the public repository EV-TRACK (https://evtrack.org) (EV-TRACK ID: EV220303). The mammalian methylation array is available from the Epigenetic Clock Development Foundation (https://clockfoundation.org/). Raw data from sEV miRNA analysis can be found at ExoCarta. The rest of the data needed to evaluate the conclusions in the paper are present in the paper and/or the Supplementary Materials.

Submitted 31 March 2022
Accepted 31 August 2022
Published 19 October 2022
10.1126/sciadv.abq2226